The Inclusive Jet Cross Section

using the k_{\perp} Algorithm

Sebastian Grinstein

Advisor: Ricardo Piegaia

Co-advisor: Daniel Elvira

This dissertation presents the first measurement of the inclusive jet cross section

using the k_{\perp} algorithm for reconstruction of jets in a hadron collider experiment.

The measurement uses 87.3 pb^{-1} of data collected with the DØ detector at the

Fermilab Tevatron $p\bar{p}$ Collider during 1994–1995. The cross section, reported as a

function of transverse momentum $(p_T > 60 \text{ GeV})$ in the central region of pseudo-

rapidity ($|\eta| < 0.5$), exhibits reasonable agreement with next-to-leading order

QCD predictions, except at low p_T where the agreement is marginal. Comparisons

with results based on the cone algorithm are also presented. Both data and Monte

Carlo simulations indicate that k_{\perp} (D=1) jets encompass more energy than cone

(R=0.7) jets, this energy difference accounts for the difference between the k_{\perp} and

cone cross sections.

Keywords: Quantum cromodynamics, Jet cross section, k_{\perp} algorithm.

2003

Acknowledgments

In the first place I have to thank my advisor, Ricardo Piegaia. Through these years he was always, and still is, willing to explain and discuss any topic, including those not related with physics. During the many times that we spent long hours working together I have learn a lot, and I am still surprised by his vast knowledge on high energy physics. I have been extremely lucky to have him as an advisor.

I am also deeply grateful to my co-advisor, Daniel Elvira. With his experience he has guided me through all the many steps required to carry out a physics analysis at $D\emptyset$. His advice was always concrete and useful. I have experience the meaning of the words "cross check" thanks to his devotion to quality results. This analysis would not have been finished, ie, published, without his guidance.

Working with Gaston Gutierrez was one of my most valuables experiences during my time at $D\emptyset$. With him, I had the opportunity to work on and learn about critical issues of the experiment. Gaston showed me, by example, that by working hard enough most problems can be resolved. I am also very much in debt for his skiing lessons at Devil's Head.

Of the many people that have helped me through this work, I am specially grateful to Levan Babukhadia and Robert Snihur. Their work as graduate students paved the way for this analysis. Both were always willing to help me and share their experiences (and code!).

I would like to thank the Editorial Board of the analysis (Anna Goussiou, Iain Bertram, Drew Baden, Bob Hirosky, Aurelio Juste and Bernard Pope). Specially

Anna, who took the time to correct the many versions of the notes and drafts and suggest important improvements.

Special thanks to the QCD conveners, John Krane and Marek Zielnski. I am grateful for their support and suggestions during the different stages of the analysis. I would also like to thank the DØ spokepersons, Harry Weerts and John Womersley, and specially Gene Fisk for the support I had during my stay at Fermilab.

Contents

1	Jet Physics							
	1.1	Quantum Chromodynamics	2					
	1.2	Jets in Hadron Colliders	4					
	1.3	Jet Definition	9					
		1.3.1 Jet Kinematics	11					
		1.3.2 The Fixed Cone Algorithm	12					
		1.3.3 The k_{\perp} Algorithm	15					
	1.4	The Inclusive Jet Cross Section	19					
	1.5	Theoretical Predictions						
		1.5.1 Cone and k_{\perp} Algorithms at NLO	22					
	1.6	Monte Carlo Simulations	24					
2	Exp	perimental Apparatus	27					
	2.1	The Fermilab Tevatron	27					
	2.2	The DØ Detector	28					
		2.2.1 The Central Detectors	31					
		2.2.2 The Calorimeter	32					
		2.2.3 The Muon System	37					
		2.2.4 The Level \emptyset Detector	37					
	2.3	Detector Simulation	38					

3	Dat	a Collection and Event Reconstruction	40				
	3.1	Data Collection	40				
		3.1.1 The Level Ø Trigger	41				
		3.1.2 The Level 1 Trigger	42				
		3.1.3 The Level 2 Trigger	43				
		3.1.4 The Jet Triggers	44				
	3.2	Offline Reconstruction	44				
		3.2.1 Determination of the Interaction Vertex	46				
		3.2.2 Missing Transverse Energy	46				
		3.2.3 Jet Reconstruction Algorithms	47				
		3.2.4 Calorimeter Cell Restoration	49				
		3.2.5 The H_T Correction	50				
4	Dat	a Selection and Associated Efficiency	52				
	4.1	2.1 Cut Efficiency Calculation					
	4.2	Event Selection	53				
		4.2.1 The Vertex z Position Cut	54				
		4.2.2 The Missing Transverse Energy Cut	54				
	4.3	Jet Selection	56				
5	Jet Momentum Calibration						
	5.1	Momentum Scale Correction	59				
		5.1.1 Offset Correction	60				
		5.1.2 Jet Response	63				
	5.2	Width dependence of the Response	64				
	5.3	Misclustering					
	5.4	Monte Carlo Closure	66				
6	Jet	Momentum Resolutions	69				

	6.1	Determination of the Jet Momentum			
		Resolutions			
		.1.1 Soft Radiation Correction			
		1.1.2 Particle Level Imbalance Subtraction			
		$7.1.3$ k_{\perp} Resolutions			
	6.2	Monte Carlo Closure Test			
	6.3	Consistency Checks			
		3.3.1 Cone Consistency Check			
		3.3.2 Cross Checks of the Monte Carlo Closure Test			
		3.3.3 Plate Level k_{\perp} and Cone Straight Resolutions 80			
		3.3.4 Comparison between k_{\perp} and Cone resolutions 82			
	6.4	Conclusions			
7	The	Inclusive Cross Section 88			
	7.1	Juminosity Determination			
		7.1.1 Trigger Thresholds			
		7.1.2 Trigger Matching			
	7.2	The Observed Inclusive Jet Cross Section			
	7.3	Unfolding of the Cross Section			
	7.4	Final Inclusive k_{\perp} Jet Cross Section			
		7.4.1 Relative Importance of the Corrections			
	7.5	Experimental Uncertainties			
8	Con	parison with Theory and Analysis of the Results 103			
	8.1	Oata and Theory Comparison			
	8.2	The Cone Inclusive Jet Cross Section			
	8.3	g_{\perp} and Cone Jets at High p_T			
	8.4	${f c}_{\perp}$ and Cone Jet Cross Sections			
		4.1 Comparing individual k_1 and Cone Jets in the Data 109			

В	Uno	lerlyin	g Event Correction Studies	127
A	\mathbf{Pre}	cluster	ring Studies	125
	8.6	Concl	usions	124
			NLO QCD Theoretical Predictions	122
		8.5.1	Including Hadronization in the	
	8.5	Hadro	nization Effects	117
			in Monte Carlo	116
		8.4.3	Comparing global production of k_{\perp} and Cone Jets	
			in Monte Carlo	115
		8.4.2	Comparing individual k_{\perp} and Cone Jets	

Chapter 1

Jet Physics

The quark model, which describes hadrons as composite particles, was first proposed in the early 1960s [1] and was confirmed in a series of experiments at the Stanford Linear Accelerator Center in the late 1960s and early 1970s. The model developed into the theory of strong interactions, quantum chromodynamics or QCD [2], which describes the interactions of quarks and gluons. Together with the theory of electroweak interactions, QCD forms the foundation of the standard model of particle physics. Perturbative QCD predicts the jet production cross section at large transverse momentum from quark and gluon scattering in hadron collisions. The outgoing quarks and gluons, collectively called partons, hadronize to form jets of particles. High transverse momentum jets were first observed at the CERN Intersecting Storage Rings (IRS) [3]. The measurement of the inclusive jet cross section can be used to test the predictions of perturbative QCD, study the proton structure, and look for quark compositness. In order to facilitate comparisons between data and theoretical predictions, jet defining algorithms are used by both experiments and theoreticians. Jets can be defined in the detector level, as clusters of energy deposits, and in Monte Carlo simulations or perturbative QCD calculations as final state hadrons or outgoing partons from the hard subprocess. A suitable jet algorithm should not be sensitive to the type of objects to which it is applied. Clustering algorithms, such as the k_{\perp} algorithm [4, 5, 6, 7], offer advantages over cone based algorithms which have been previously used in hadron colliders. This analysis presents the first measurement of the inclusive jet cross section using the k_{\perp} algorithm to reconstruct jets at the $\sqrt{s} = 1.8$ TeV Tevatron proton-antiproton collider.

After a brief introduction to quantum chromodynamics, this chapter discusses the jet production process, jet definition, and the inclusive jet cross section at hadron colliders.

1.1 Quantum Chromodynamics

The Standard Model [8] (SM) of particle physics is a term used to describe the quantum theory that includes the theory of strong interactions (quantum chromodynamics or QCD) and the unified theory of weak and electromagnetic interactions (electroweak). The SM describes nature at very small distance scales, typically scales smaller than that of an atomic nucleus ($\sim 10^{-15}$ m). Mathematically, the standard model is a theory of interacting quantum fields. Excitations in these fields correspond to particles, and each separate field corresponds to a different type (or flavor) of a particle. These particles can be classified in three groups: quarks, leptons, and gauge bosons. Table 1.1 lists the standard model particles and their properties. The quarks and leptons, which are all spin-1/2 particles and thus obey the Pauli exclusion principle, make up what is usually thought of as "matter". Both the quarks and leptons are grouped into three generations of two particles each. The corresponding particles in each generation have similar properties, except for their masses, which increase with each successive generation. All "normal" matter (protons, neutrons, and electrons) is composed of particles from the first generation (electron and u and d quarks). Particles in higher generations can be produced in high-energy interactions (such as when cosmic rays hit the

	Symbol	Name	Mass (GeV)	Charge (e)
Quarks	u	up	0.003	2/3
$(spin = \frac{1}{2})$	d	down	0.006	-1/3
	c	$_{ m charm}$	1.3	2/3
	s	$\operatorname{strange}$	0.1	-1/3
	t	top	175	2/3
	b	bottom	4.3	-1/3
Leptons	e	electron	0.0005	-1
$(spin = \frac{1}{2})$	$ u_e$	electron neutrino	$< 3 \mathrm{~eV}$	0
	μ	muon	0.106	-1
	$ u_{\mu}$	muon neutrino	$< 0.19~{ m MeV}$	0
	au	tau	1.777	-1
	$ u_{ au}$	tau neutrino	< 0.02	0
Gauge bosons	γ	photon	0	0
(spin = 1)	W	W	80	±1
	Z	Z	91	0
	g	gluon	0	0
SM Higgs boson	H^0	Higgs	?	0

Table 1.1: Particles of the standard model [9].

upper atmosphere), but they are unstable and ultimately decay into first generation particles or photons. The proton is made of two u quarks and a d quark. These three quarks that give the proton its identity are called valence quarks. The valence quarks interact strongly inside the proton exchanging gluons which may create quark and antiquarks pairs known as "sea" quarks.

The gauge theory of electromagnetism, Quantum Electrodynamics or QED, describes the interaction of charged particles through the mediating gauge boson, the photon. Similar to QED, Quantum Chromodynamics describes the strong interactions of quarks through its gauge bosons, the gluons. In strong interactions color charges interact according to the dynamics of the SU(3) group. Three strong

charges exist, the label "color" was applied to them since the combination of the three (red, blue, green) yields a total neutral charge. Quarks carry a single color while gluons carry a non-singlet combination of color and anticolor charges. Gluons are massless but, unlike the photon, can interact with each other. The strength of the chromodynamic interaction is set by the strong coupling constant α_s . One remarkable feature of QCD is its asymptotic freedom, the strong coupling gets weaker at shorter distances or at higher momenta (Q^2). On the other hand, at low momenta or large distances, the strong coupling strength increases, confining quarks and gluons inside colorless objects called hadrons. This is the origin of the concept of color confinement [10], responsible for the jet production.

In the framework of QCD, predictions for scattering processes are obtained by perturbative methods using the Feynman rules which can be derived from the Lagrangian density. The cross section of any QCD process can be calculated as a power series in the strong coupling constant. The contributions of each order can be represented by Feynman diagrams, each of which is a combination of fundamental interaction vertices joined by propagators. The fundamental vertices of QCD are shown in Figure 1.1. Quarks are represented by straight solid lines and gluons by helixes. The four gluon vertex contributes a factor of α_s in the Feynman diagram while the other two vertices a factor of $\sqrt{\alpha_s}$. A given cross section is obtained as the absolute value squared of the sum of all contributing matrix elements integrated over the available phase space.

1.2 Jets in Hadron Colliders

High energy hadron collisions result in the scattering of their constituents, quarks and gluons. The QCD coupling constant becomes small at high energies (small distances) as a consequence of asymptotic freedom. Thus, the hard scattering among partons can be calculated using the perturbative techniques of the quantum

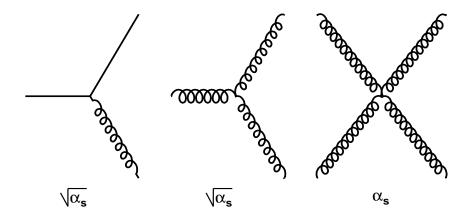


Figure 1.1: The fundamental QCD vertices.

field theories. However, color confinement does not allow a direct experimental test of the parton level hard scattering. As the distance between the hard scattered partons increases, the strong coupling potential grows large enough to generate dozens of gluons and quark-antiquark pairs. These quarks and gluons ultimately recombine into stable, colorless particles. This last non perturbative process, known as hadronization or fragmentation, results in showers of collimated particles called jets.

The perturbative component of the hard scattering can be calculated analytically. Feynman diagrams can be used to represent the contribution of each order. Figure 1.2 shows some $2 \to 2$ α_s^2 (a), $2 \to 2$ α_s^3 (b), and $2 \to 3$ α_s^3 (c) diagrams. Table 1.2 lists all possible $2 \to 2$ subprocesses with their invariant amplitudes. Leading order perturbative calculations do not include any internal loops. However, at higher orders in α_s , loop integrals become divergent at large momenta. These ultraviolet divergences can be isolated by the regularization procedure, either by introducing a momentum cut-off or by dimensional regularization [11]. The regularized divergences are then removed by absorbing them into the definition of the coupling strength via the renormalization procedure, which introduces a new scale, the renormalization scale, μ_R .

After the hard scattering the parent hadrons loose the color charge of the interacting partons. As a result the remnant of the initial hadrons undergo hadronization also. The additional hadronic products resulting from the spectator partons, which do not participate in the hard scattering, are collectively called the underlying event.

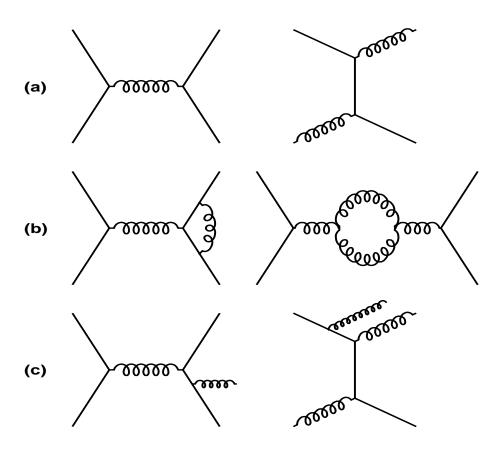


Figure 1.2: Example of some QCD processes: $2 \to 2$ leading (a) and next-to-leading (b) orders, $2 \to 3$ processes of α_s^3 order (c).

In a hadron collision, the fraction of the hadron's momentum carried by each parton, referred to as Bjorken x, $x = p_{parton}/p_{hadron}$, is not known. However, for a given hadron, the distribution of the momenta of the various constituent partons can be determined. Since interactions of partons inside hadrons take place at low

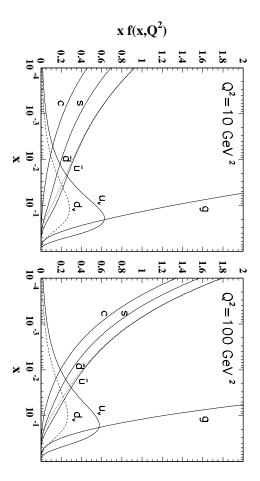
Subprocess	$ M(90^{\circ}) ^2/16\pi^2\alpha_s^2$
$qq' \rightarrow qq'$	2.2
$q\bar{q}' o q\bar{q}'$	2.2
$qq \rightarrow qq$	3.3
$q\bar{q} \to q'\bar{q}'$	0.2
$q\bar{q} \to q\bar{q}$	2.6
$q\bar{q} o gg$	1.0
$gg o qar{q}$	0.1
qg o qg	6.1
gg o gg	30.4

Table 1.2: List of all possible $2 \to 2$ processes in QCD and their invariant amplitudes (q and q' indicate different quark flavors).

energies, perturbation theory is not applicable. Instead, parametrizations of the so-called "parton distribution functions" (PDF's), $f_{i/h}(x)$, give the momentum distributions of the parton, i, inside the hadron, h. The PDF's are independent of the specific interaction and can be experimentally measured. The best knowledge of the PDF's is obtained from global fits to a large number of data sets which are separately sensitive to different parton flavors or to different linear combinations of parton flavors.

Any cross section involving partons in the initial state is given by the product of the parton distribution function and the partonic cross section, summed over all contributing partons and integrated over all values of x. This procedure is called factorization of the perturbative (high energy) and non-perturbative (low energy) processes. By introducing a new scale, the factorization scale, μ_F , the parton distribution functions can absorb initial state collinear divergences not solved by renomalization. Since PDF's can be measured only at a finite number of momentum transfer scales, Q^2 , the Dokshitzer-Gribov-Lipatov-Altarelli-Parisi (DGLAP) equations are used to evolve the parton distribution functions to mo-

Figure 1.4 for the CTEQ4M PDF's. At low energies, jet production is dominated family. The relative contributions of the different subprocesses is best shown in quarks and gluons inside the proton at $Q^2 = 10$ and 100 GeV^2 of the CTEQ [12] mentum regions where data does not exist. Figure 1.3 shows the PDF's of light quark-quark scattering. by gluon-gluon and quark-gluon scattering, while at high energies it is largely



the differences between them. $Q^2 = 10$ and 100 GeV². The PDF's are weighted by the Bjorken x to highlight Figure 1.3: The CTEQ4M PDF's for quarks and gluons inside the proton at

imentally measured jet cross section and the theoretical calculations thus reveals sections can be calculated based on parton distribution functions and the matrix the structure of the proton as well as tests the perturbative QCD predictions for elements of the elementary parton processes. work to study the jet production process. Theoretical predictions for the jet cross antiprotons collide at a center of mass energy of 1.8 TeV, offers an excellent frameter of mass energies above 10 GeV. The Fermilab Tevatron, where protons and Jet production is the dominant process in hadron-hadron collisions with cen-The comparison between the

the hard scattering.

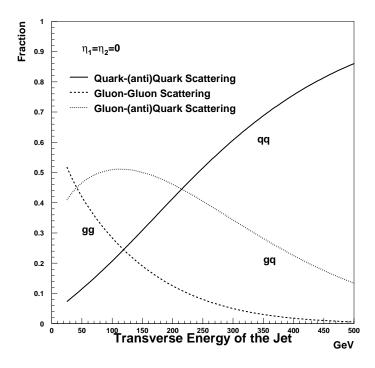


Figure 1.4: Contributions of the various subprocesses to the inclusive jet cross section, from [13].

1.3 Jet Definition

In hadron collider experiments the distributions of final state quarks and gluons can not be measured. Owing to color confinement the final state objects of the reaction are colorless hadrons. In order to study the parton level interactions, event properties which are weakly affected by long distance processes and which have a close correspondence between partonic and hadronic final states are desirable. The concept of jets was introduced to allow comparisons between the elementary quarks and gluons and the hadrons observed in final states of high energy collisions. In general, jet definitions (jet algorithms) must be:

- 1. Fully specified. The jet selection process, jet kinematic variables and the various corrections should be clearly defined.
- 2. Theoretically well behaved. The algorithm should be infrared and collinear safe, with no ad-hoc parameters.
- 3. Detector independent. There should be no dependence on detector type, size, segmentation, etc.
- 4. Consistent. The algorithm should behave equally at the theoretical and experimental levels.

The first two criteria should be satisfied by every algorithm. The last two, however, can probably never be totally true, since it is not possible to completely remove the dependence of the measurements on the experimental apparatus.

For an observable to be calculable in perturbative QCD and also in order to reduce the experimental sensitivity to positional resolution and detector trigger thresholds, jet algorithms should be:

- Infrared safe: insensitive to emission of low energy particles. The jet observable should not change by adding an additional particle with $E \to 0$ to the final state.
- Collinear safe: the jet observable should not change when replacing a pair of particles by a single particle carrying the summed momentum.

In a typical hard scattering event an outgoing parton generates a shower of quarks and gluons, these quarks and gluons hadronize into particles which interact with the detector and are thus "detected" through electronic signals in the apparatus. Figure 1.5 shows a diagram of the jet evolution. The scattered partons generate more quarks and gluons as they emerge from the interaction point, a process known as parton showering, the hadronization process that follows ends with

a shower of particles which finally enter the detector. Jet algorithms should yield similar results if applied to any of these steps. Experiments typically correct their measurements from the detector to the particle level, *i.e.* before the shower of particles interact with the detector. The theoretical predictions are usually made at the parton level, including only the lowest order contributions. At hadron colliders, the non perturbative process of hadronization is regarded as not important, in the sense that it does not modify the jet observables.

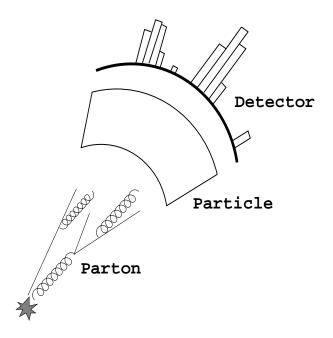


Figure 1.5: Graphical representation of the evolution of a jet: parton, particle and detector levels.

1.3.1 Jet Kinematics

Although hadron collisions at symmetric colliders occur in their center of mass (CM) frame, the constituent partons undergoing the hard interaction are not generally in their CM frame, the fraction of the momentum carried by each interacting parton varies from event to event. As a result the CM system is randomly boosted from event to event along the direction of the colliding hadrons. The

usual variables, energy, E, and momentum, \vec{p} , are not convenient to describe the hard collision. Jets are usually described by the relativistically invariant (under longitudinal boosts) variables: transverse momentum (p_T) , azimuth angle (ϕ) , rapidity (y), and mass (m). Jet rapidity is defined as:

$$y = \frac{1}{2} \ln \frac{E + p_z}{E - p_z} = \tanh^{-1} \left(\frac{p_z}{E}\right)$$
 (1.1)

which under a Lorentz boost along the direction of the colliding particles to a frame with velocity β , transforms as $y \to y - \tanh^{-1} \beta$, yielding a boost-independent distribution dN/dy. In the high energy limit, when $p \gg m = \sqrt{E^2 - p^2}$,

$$y \approx -\ln\left[\tan\left(\frac{\theta}{2}\right)\right] \equiv \eta$$
 (1.2)

which defines pseudo-rapidity, η , as a purely angular coordinate. In a collider experiment, the directly measured jet quantities are energy (E), pseudo-rapidity and azimuth.

1.3.2 The Fixed Cone Algorithm

Historically, cone algorithms have been used for jet definition in $p\overline{p}$ colliders. The Snowmass Accord [14] attempted to provide a standardized definition across experiments and theory, defining jets as cones which maximize the energy within an area $A = \pi R^2$ in $\eta - \phi$ space, where R is the cone radius. However, this definition has proven to be incomplete when applied to experimental data or Monte Carlo simulations. First, in order to reduce the computer processing time required by the algorithm, local maximization is used, starting from "seeds" directions. Secondly, the Snowmass Accord does not deal with jet overlap. As a consequence, there is no unique cone algorithm, the different implementations mainly differ in how the case of overlapping cones is treated. In this analysis the DØ implementation of the fixed cone algorithm will be discussed [15].

The DØ cone algorithm starts with a list of detector preclusters (see section 3.2.3), or particles or partons in a Monte Carlo simulation. These will be

collectively referred to as "vectors". Jets are defined in two sequential procedures. In the first, or clustering, procedure, vectors that belong to a jet are accumulated, and in the second the η , ϕ and transverse energy of the jet are defined. The fixed cone algorithm is an iterative algorithm which starts about the most energetic vectors in the event (seeds). Seeds define the starting jet direction or jet axis (η_{jet}, ϕ_{jet}) . The algorithm process as follows:

1. All vectors in a cone of size R around the jet axis are summed, the transverse energy, E_T , of the jet is defined as the sum of the transverse energies of the vectors included in the jet:

$$E_T = \sum_{i \in R_i < R} E_{T,i} = \sum_{i \in R_i < R} E_i \sin \theta_i \tag{1.3}$$

and the jet direction recalculated using the Snowmass [14] convention:

$$\eta_{jet} = \frac{1}{E_T} \sum_{i \in R_i < R} E_{T,i} \eta^i \qquad \phi_{jet} = \frac{1}{E_T} \sum_{i \in R_i < R} E_{T,i} \phi^i$$
(1.4)

- 2. Step 1 is iterated until the jet direction is stable.
- 3. Finally, overlapping jets are merged or split according to the following criteria: two jets are merged into one if more than a fraction, f (arbitrarily chosen f = 50% at DØ), of the E_T of the jet with the smaller E_T is contained in the overlap region. Otherwise the vectors in the overlap region are assigned to the nearest jet and the direction and transverse energy of these jets are recalculated following equation 1.7.

The reconstruction process of the DØ jet cone algorithm is completed with the calculation of the kinematic variables associated with each jet. The DØ jet algorithm and the Snowmass algorithm calculate the final direction of the jet differently [15]. For each vector the basic quantities are: energy (E_i) , azimuth angle (ϕ_i) and polar angle (θ_i) . The energy of the jet is defined as:

$$E = \sum_{i} E_i \tag{1.5}$$

where the sum is over the jet's vectors. Assuming massless vectors the jet momentum components are defined following:

$$p_x = E_x = \sum_i E_i \sin \theta_i \cos \phi_i$$

$$p_y = E_y = \sum_i E_i \sin \theta_i \sin \phi_i$$

$$p_z = E_z = \sum_i E_i \cos \theta_i$$
(1.6)

The jet centroid is given by:

$$\phi = \tan^{-1}\left(\frac{E_y}{E_x}\right) \qquad \theta = \tan^{-1}\left(\frac{\sqrt{E_x^2 + E_y^2}}{E_z}\right) \tag{1.7}$$

and the jet pseudo-rapidity is calculated using equation 1.2. The jet transverse energy is obtained from equation 1.3 while the transverse momentum is given by:

$$p_T = \sqrt{p_x^2 + p_y^2} (1.8)$$

which is different from the jet E_T as defined in equation 1.3.

Previous QCD analyses from hadron colliders based on the cone algorithm set the jet cone size to R=0.7. This is an optimal value from the experimental point of view, because while it provides good shower containment it minimizes contamination. From the theoretical point of view, this cone size is desiarable because calculations at α_s^3 are stable (do not depend on the factorization and renormalization scales) [16].

Two issues complicate the picture of cone jets. The precise definition of the seeds makes the merging step sensitive to soft radiation [17]. On the other hand, an additional parameter has to be introduced in the theoretical calculations, to simulate the role of seeds and the merging/splitting rules.

The infrared unsafeness of the cone algorithm manifests itself in cross sections calculated at next-to-next-to-leading order (NNLO). Consider two well separated partons that fit inside, but on opposite sides, of a single cone, as shown in Figure 1.6. With only the two partons, and nothing else to serve as a seed, the cone

algorithm described above will reconstruct two jets. At NNLO a very soft gluon could be radiated between the partons and serve as a seed. In this case the cone algorithm will reconstruct a single jet. Thus the outcome of the cone algorithm with seeds is sensitive to soft radiation ¹. The cone algorithm used in theoretical predictions will be discussed in section 1.5.1. The k_{\perp} algorithm, described below, is infrared safe and defines jets in the same way at theoretical and experimental levels.

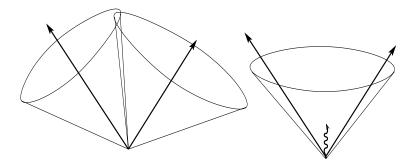


Figure 1.6: An illustration of infrared sensitivity in cone clustering. The presence of soft radiation between the two jets may cause the merging of the jets that would otherwise not occur.

1.3.3 The k_{\perp} Algorithm

Clustering algorithms have been widely used in e^+e^- colliders. In contrast to cone algorithms, which globally find the jet direction, clustering algorithms successively merge pairs of nearby vectors. The order in which vectors are recombined into jets defines the algorithm. Traditionally, invariant mass was used as the ordering variable, but this leads to a non intuitive combination of soft vectors separated by wide angles. The k_{\perp} algorithm overcomes this difficulty by combining vectors based on their relative transverse momentum.

¹The cone algorithm with "midpoints" solves the infrared safeness problem [18].

Several variants of the k_{\perp} algorithm for hadron colliders have been proposed [4, 5, 6], The main difference between them concerns when the recombination process stops. DØ implemented the Ellis and Soper [6] criteria based on its flexibility and because it allows relatively simple comparisons with previous results obtained with the fixed cone algorithm.

A desirable feature of a jet algorithm is the association of collinear vectors and soft vectors to the harder parent vector. The k_{\perp} algorithm associates particles with low $d \approx min(p_{T,A}^2, p_{T,B}^2) \times \Delta R_{AB}^2$, so the parameter which determines if two particles are going to be merged or not, is proportional to the softness of the two particles, the minimum p_T squared, and proportional to the collinearity of the particles, their separation in $\eta - \phi$ space.

The k_{\perp} algorithm successively merges pairs of vectors in order of increasing relative transverse momentum. The algorithm contains a single arbitrary parameter, D, that controls when the merging stops. The k_{\perp} algorithm starts from a list of vectors, which can be detector preclusters (see section 3.2.3), particles or partons in a Monte Carlo simulation, or partons in a perturbative QCD calculation. The recombination procedure is as follows:

1. For each pair of vectors, i and j, define:

$$d_{ij} = min(p_{T,i}^2, p_{T,j}^2) \frac{\Delta R_{ij}^2}{D^2}$$
(1.9)

where $\Delta R_{ij}^2 = (\eta_i - \eta_j)^2 + (\phi_i - \phi_j)^2$. For each vector define:

$$d_i = p_{T,i}^2 (1.10)$$

For D=1 and $\Delta R_{ij}\ll 1$, d_{ij} is the squared of the relative transverse momentum (k_{\perp}) between the vectors.

2. The minimum, d_{min} , of all d_i and d_{ij} is found.

3. If d_{min} is a d_{ij} then the vectors are merged, using the four-vector recombination scheme (or *E*-scheme), into a new vector k with:

$$E_k = E_i + E_j \qquad \vec{p}_k = \vec{p}_i + \vec{p}_j$$
 (1.11)

- 4. If d_{min} is a d_i (ie, $\Delta R_{ij}^2 > D^2$ for all j), then the vector can not be combined and it is removed from the vector list and added to the jet list.
- 5. Steps 1-5 are repeated until all the vectors have been merged into jets.

The rest of the kinematic variables of the resultant jets are determined from:

$$\theta = \tan^{-1} \left(\frac{\sqrt{p_x^2 + p_y^2}}{p_z} \right) \qquad \phi = \tan^{-1} \left(\frac{p_y}{p_x} \right) \qquad E_T = p_T = \sqrt{p_x^2 + p_y^2} \quad (1.12)$$

and jet pseudo-rapidity from equation 1.2.

Figure 1.7 shows the algorithm process in a simplified diagram of a hadron collision. k_{\perp} jets do not have to include all vectors within a cone of radius D around the jet axis, but can contain vectors outside this cone. Since the algorithm fundamentally merges nearby vectors, there is a close correspondence of detector jets to particle jets. Every vector in the event is assigned uniquely to a jet and therefore there are no overlapping jets as there are in the cone case. The k_{\perp} algorithm is infrared and collinear safe to all orders of calculation.

In this analysis the parameter of the k_{\perp} algorithm, D, was set to D=1. This choice was made because the theoretical prediction to order α_s^3 for the k_{\perp} inclusive jet cross section with D=1 is very similar to the cone prediction with R=0.7 [6]. D=1 is also preferred theoretically as it treats initial and final state radiation in the same way and would be expected to give the smallest higher order corrections [19].

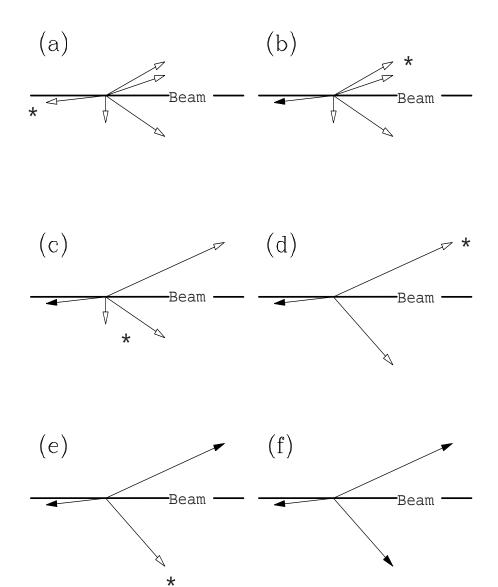


Figure 1.7: Illustration of the k_{\perp} algorithm recombination procedure for a simplified example of a hadron collision final state. The open arrows represent vectors in the event, and the solid ones the final jets reconstructed by the k_{\perp} algorithm. The six diagrams show successive iterations of the algorithm. In each diagram either a jet is defined, or two vectors are merged. The asterisk marks the relevant vector at each iteration.

1.4 The Inclusive Jet Cross Section

The most direct test of perturbative QCD is the measurement of the inclusive jet cross section. In $p\overline{p}$ collisions the inclusive cross section is determined from the process:

$$p\,\bar{p} \to jet + \text{anything}$$
 (1.13)

In the framework of the parton model, the total cross section for this reaction can be factorized into components from the empirically determined PDF's, f, and perturbative calculated two-body scattering cross section, $\hat{\sigma}$. This hadronic cross section is given by:

$$\sigma(1+2 \to jet + \text{anything}) = \sum_{ij} \int dx_1 \, dx_2 \, f_i(x_1, \mu_F^2) \, f_j(x_2, \mu_F^2)$$

$$\times \hat{\sigma}[x_1 \, p_1, x_2 \, p_2, \alpha_s(\mu_R^2), \frac{Q^2}{\mu_F^2}, \frac{Q^2}{\mu_R^2}] \tag{1.14}$$

where the index i refers to the type of parton (quarks or gluons), $f_{i(j)}(x_{1(2)}, \mu_F^2)$ represent the parton distribution functions of the proton (antiproton) defined at factorization scale μ_F , $p_{1(2)}$ is the momentum of the proton (antiproton), $x_{1(2)}$ is the fraction of the proton (antiproton) momentum carried by the scattered parton, and μ_R is the renormalization scale. The measurement of the inclusive jet cross section tests the perturbative QCD predictions as well as the proton structure, the parton distribution functions. Parton compositness is also tested by this measurement, if quarks and gluons have a substructure the parton-parton scattering amplitudes given by QCD would be modified causing a deviation in the cross section at the highest energies [20]. A simplified diagram of proton-antiproton interaction is shown in Figure 1.8.

It is, however, impossible to measure the total jet cross section in an experiment, since jets are counted only in the fiducial volume of the detector. No attempt is made to extrapolate the measurements to regions not covered by the detector. Moreover, due to trigger and reconstruction inefficiencies, it is prac-

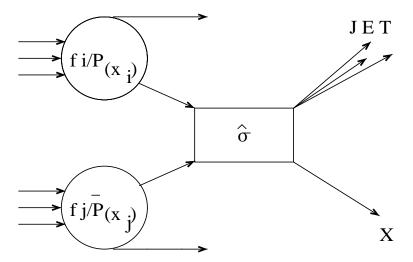


Figure 1.8: Description of the jet production process in a hadron collider. The parton distribution functions, f(x), give the probability to find a certain parton carrying a fraction x of the proton momentum. The elementary interaction, $\hat{\sigma}$, can be calculated with perturbative QCD.

tically impossible to accurately measure the lowest energy region of the cross section. Experiments thus measure the differential cross section in jet transverse momentum and pseudorapidity intervals. This analysis presents the double differential inclusive k_{\perp} jet cross section, measured with the DØ detector, defined as:

$$\frac{d^2\sigma}{dp_T d\eta} (p\overline{p} \to jet + X) \tag{1.15}$$

Jets are selected in the pseudorapidity range of $|\eta| < 0.5$ and binned in terms of transverse momentum, p_T . The measurement is compared to next-to-leading order theoretical predictions, discussed in the next section.

1.5 Theoretical Predictions

The measured jet cross section is compared to next-to-leading order (NLO) theoretical predictions, which include all terms of third order in α_s but does not include hadronization effects. As discussed in section 1.2, the need to remove ultraviolet divergences in the perturbative calculation of the parton scattering cross section, introduces a new scale, the renomalization scale, μ_R . In addition, an arbitrary factorization scale, μ_F , is needed to remove the infrared divergences. Both the parton distribution function and the parton scattering cross section depend on the factorization scale. Qualitatively, μ_F represents the scale that separates the short and long range processes. The scales μ_F and μ_R should be chosen of the same order as the hard scale of the interaction, Q. The larger the number of terms included in the perturbative expansion the smaller the dependence on these scales. Typically, μ_F and μ_R are set to the same value, $p_T^{max}/2$, where p_T^{max} refers to the p_T of the leading jet in an event.

Several perturbative NLO QCD calculations are available [21, 22]. In this analysis the event generator JETRAD [22] is used. The program requires the selection of renormalization and factorization scales, a set of parton distribution functions, and a jet clustering algorithm. Parton distribution functions of the CTEQ [12] and MRST [23] families are considered in this analysis. Figure 1.9 shows the QCD prediction for the inclusive jet cross section using the k_{\perp} algorithm for the pseudorapidity interval of $|\eta| < 0.5$ for different parton distribution functions at a center of mass energy of $\sqrt{s} = 1.8$ TeV. The same definition of the k_{\perp} algorithm can be used on NLO QCD predictions and collider data, no modifications or additional parameters have to be introduced.

Although the matrix elements for the two loop $2 \to 2$ scattering have recently been calculated [24], the Next-to-Next-to-leading order prediction (α_s^4) for the inclusive jet cross section is not available yet.

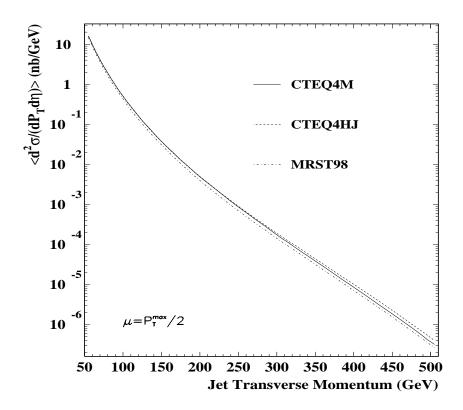


Figure 1.9: JETRAD QCD prediction for the spectrum of the inclusive jet cross section using the k_{\perp} algorithm as a function of transverse momentum for different parton distribution functions.

1.5.1 Cone and k_{\perp} Algorithms at NLO

The cone jet definition suffers from ambiguities related to the merging and splitting process and the starting seeds of the algorithm. Further problems arise when trying to make comparisons between collider data and theoretical predictions. In perturbative QCD calculations of parton-parton scattering at leading order (LO, $\mathcal{O}(\alpha_s^2)$) there are two partons in the final state. These partons are well separated and always yields two jets in the final state. At NLO there can be up to two partons in a jet. Initially, the Snowmass convention was used to define cone jets in theoretical calculations. At NLO this convention will always combine two partons into a single jet if their distance in $\eta - \phi$ space is less than 2R. However,

experimentally, the two partons evolve and hadronize. The resultant configuration could produce more than one jet depending on the splitting and merging criteria.

In order to accommodate the differences between jet definitions at parton and experimental levels, an ad-hoc parameter, R_{sep} [25], the maximum distance between partons inside a jet divided by the cone size, was introduced. This algorithm, referred to as the modified Snowmass algorithm (illustrated in Figure 1.10), requires final state partons to be within one cone width, R, of the jet direction, and within R_{sep} cone widths of one another, in order to be combined into a single jet.

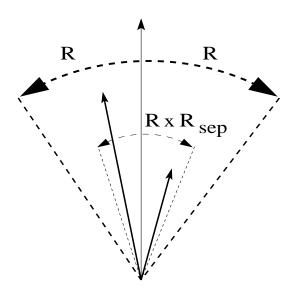


Figure 1.10: The modified Snowmass cone algorithm used to make NLO QCD predictions. The full arrows represent partons which, if within $R \times R_{sep}$ of each other, are combined into a single jet.

The R_{sep} parameter was tuned to the data, the value of $R_{sep} = 1.3$ was found to best simulate the DØ merging and splitting criteria [25]. Jet cross sections predictions from the Collider Detector at Fermilab [13] (CDF) are also based on this value of R_{sep} . However, while the inclusive cross section is relative insensitive to the choice of R_{sep} [16] (a $\approx 10\%$ effect is seen when it is increased from 1.3R

to 2R), jet shapes results from the ep collider experiment at DESY, ZEUS [26], which are specially sensitive to jet structure, indicate that R_{sep} vary as a function of transverse energy and rapidity [27].

The R_{sep} procedure is not completely satisfying. Experimentally one observable is measured but compared with the calculation for another. It is not obvious how to generalize the procedure to higher orders. On the other hand, since the cone algorithm defined in the experiment is not infrared safe, there is no way of knowing the size of the non perturbative corrections [28].

Since the k_{\perp} algorithm uniquely assigns each vector to a jet, there is no need for an ad-hoc parameter, and is infrared and collinear safe to all orders of calculation. At leading order, with two partons in the final state, the k_{\perp} and cone algorithms yield identical results which do not depend on the algorithms parameters. At NLO, where there can be up to three partons in the final state, the k_{\perp} algorithm with D=1 yields basically the same result as R=0.7 ($R_{sep}=1.3$). Figure 1.11 shows k_{\perp} and cone predictions using JETRAD with the CTEQ4M PDF. At higher orders the correspondence between D=1 and R=0.7 does not have to be true.

It is important to emphasize that while there is a one to one correspondence between partons and jets in leading order perturbative calculations, experiments measure an event property that is determined by the primary partons, but not these partons themselves. Theoretical predictions contain up to three partons in the final state and do not include hadronization processes.

1.6 Monte Carlo Simulations

Monte Carlo event generators of high energy processes are widely used in high energy physics experiments. In this analysis, HERWIG [29], a general purpose event generator with parton showers simulation and cluster hadronization, is employed. Different parton distribution functions can be used with the program and

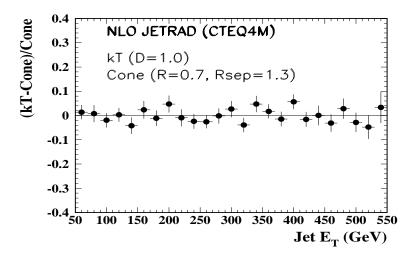


Figure 1.11: Ratio of k_{\perp} over cone JETRAD theoretical predictions at NLO (the errors shown are statistical).

the underlying event contribution can be optionally suppressed. HERWIG provides a variety of elementary hard processes, including QCD, electroweak and supersymmetric ones. Only samples generated with the elementary QCD $2 \rightarrow 2$ process were used in this analysis.

Fixed order perturbative calculations fail to predict details of the jet structure observed in experiments. Event generators use the "parton shower" approach to take into account higher order QCD effects. Following the leading order calculation, parton emissions are performed based on soft and collinear approximations [30], distributing the energy fractions according to the leading order DGLAP splitting functions. The parton showers are terminated when the parton momentum falls below a cut off parameter, Q_0 , which is typically set to the order of 1 GeV.

The non perturbative evolution is described by a phenomenological hadronization model which turns the final state partons into hadrons locally in phase space. The hadronization process is independent of the hard process because of the cut

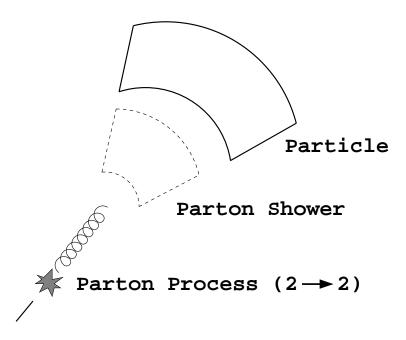


Figure 1.12: Graphical representation of the evolution of a jet in Monte Carlo simulations: partons, parton shower and particles.

off of the parton cascade. HERWIG's "cluster model" for jet hadronization is based on non-perturbative gluon splitting [31]. A similar cluster model is used for soft and underlying hadronic events. Figure 1.12 shows a diagram of the evolution of a simulated event.

Though Monte Carlo simulated jet cross sections at hadron level fail to predict the shape of the experimentally measured cross sections, the simulation models well the internal jet structure, providing a critical tool for jet based analyses. Of particular interest for this analysis, it allows to perform algorithm performance studies, to compare k_{\perp} and cone jets, and to investigate the effect of hadronization on the cross section.

Chapter 2

Experimental Apparatus

This chapter presents a brief review of the Fermilab complex and the $D\emptyset$ detector. A full description of the Fermi National Accelerator Laboratory can be found in [33], while a detailed description of the $D\emptyset$ detector is given in [34]. The Fermilab accelerator and the $D\emptyset$ detector were upgraded during the years 1995 to 2000. This analysis is based on data collected before these upgrades took place. The sections that follow describe the accelerator and detector as they were during the data taking period relevant for this analysis.

2.1 The Fermilab Tevatron

The Fermilab accelerator complex is currently¹ the site of the world's highest center of mass energy proton-antiproton collider, the Tevatron. Figure 2.1 shows an overview of the accelerator complex. The Tevatron started operations in 1985, producing $p\bar{p}$ collisions with an energy of 1.8 TeV in the center of mass. The Tevatron itself is the final stage of a series of accelerators necessary to achieve this energy. First, 18 keV H⁻¹ ions from a magneton source are accelerated

¹The Large Hadron Collider (LHC), with a center of mass energy of 14 TeV will start operations in the year 2007 [35]

by a Cockroft-Walton electrostatic accelerator to 750 keV. The ions are then accelerated to 400 MeV by a 150 m long linear accelerator (Linac). The ions are then striped of the electrons by a carbon foil and injected into the Booster, a synchrotron with a radius of 75 m, where they are accelerated to 8 GeV. In the next phase, the protons are injected into the second synchrotron, the Main Ring, which has a circular diameter of 2 km and consists of 1000 magnets to bend and focus the protons. The Main Ring accelerates the protons to 150 GeV and also provides a proton beam of 120 GeV used in antiproton creation. The 120 GeV proton beam is directed onto a tungsten target producing antiprotons with a wide momentum spread. This spread is reduced in a small synchrotron, the Debuncher, and the antiprotons are sent to a storage ring, the Accumulator, where they stay until there are enough of them to transfer to the Main Ring. In the Main Ring the antiprotons are accelerated to 150 GeV. The advantage of a $p\bar{p}$ collider is that it requires only one accelerator for counter rotating beams.

The Tevatron, located in the same tunnel as the Main Ring, includes a system of 1000 super-conduction magnets operated at 5 K to bend the beams. Six bunches of 150 GeV protons and antiprotons are injected into the Tevatron and accelerated to 900 GeV. The counter rotating bunches can collide in two interactions points, BØ (CDF) and DØ every $3.5\mu s$ with a center of mass energy of $\sqrt{s} = 1.8$ TeV.

2.2 The DØ Detector

The DØ detector is a large multipurpose apparatus designed to study the physics processes resulting from $p\bar{p}$ collisions with a center of mass energy of 2 TeV. A general view of the DØ detector is shown in Figure 2.2. Fully assembled, the detector stands 13 m in height, 11 m in width, and 17 m in length, with a total weight of about 5500 tons. The detector was built to cover a wide spectrum of physics topics by providing accurate measurements to test the Standard Model

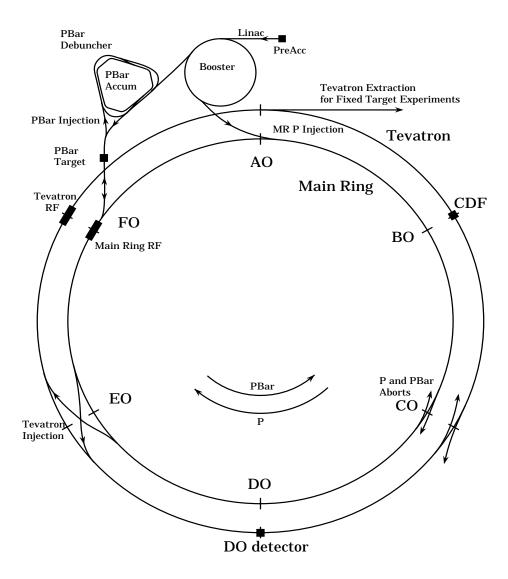


Figure 2.1: A schematic view of the Fermilab accelerator complex. Although the Tevatron and the Main Ring have the same radius, they are shown separated for clarity.

predictions and search for new phenomena. The DØ detector does not have a central magnetic field, the emphasis in the detector is on excellent calorimetry. Good measurement of high p_T jets through finely segmented, hermetic, linear and nearly compensating calorimeters, precise determination of the missing transverse energy in the calorimeters as a way of detecting neutrinos and possible other non-interacting particles, and an accurate identification and measurement of electrons and muons are the strengths of the DØ detector.

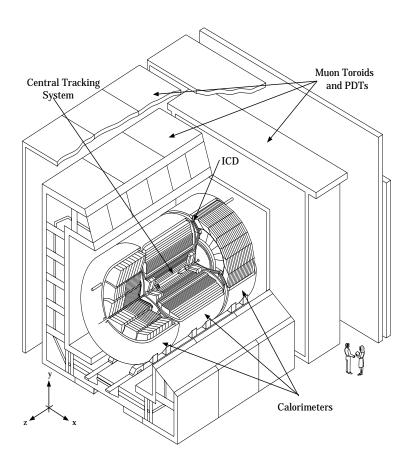


Figure 2.2: The Run I DØ detector. The support platform on which the structure rests is not shown.

The following sections describe the detector components which are relevant to

this analysis. Particular attention is paid to describing the calorimeter, which is the most important sub-detector for jet measurements.

2.2.1 The Central Detectors

The central detectors system, shown in Figure 2.3, is composed of the vertex drift chamber, the transition radiation detector and the central and forward drift chambers. The vertex chamber is the innermost drift chamber and surrounds the beam pipe. It measures the position of the interaction point in the plane perpendicular to the beam direction with a typical resolution of 50μ m. The transition radiation detector surrounds the vertex chamber and it is used to discriminate between pions and electrons. The central and forward drift chambers, the outermost sub-detectors of this system, are used to measure the trajectories of the charged particles that result from the hard scattering.

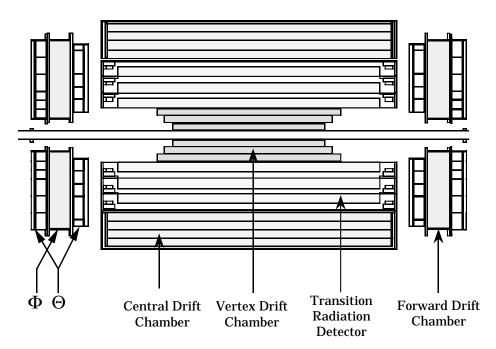


Figure 2.3: The central detectors system.

2.2.2 The Calorimeter

The calorimeter is the most important part of the DØ detector and a critical tool for jet detection. The calorimeter measures the energy of electromagnetic and hadronic showers, initiated by electrons, photons and hadrons. It is also used to determine the spatial position, direction, and in some cases, the nature of the primary particle. The missing transverse energy of the event is also measured by the calorimeter.

The DØ calorimeter, shown in Figure 2.4, is a sampling calorimeter. The electromagnetic and hadronic showers, result of the hard scattering that occurs in the center of the detector, are measured (sampled) multiple times during their development through the calorimeter. Sampling calorimeters consists of layers of grounded absorber plates, where the shower of particles loose most of their energy, inserted between signal boards (anode), all immersed in a ionizable active medium. A fraction of the total energy of the particles is deposited in the active medium, as ionization, inducing an electrical signal in the anode. This signal is calibrated to the incoming particle energy.

The DØ calorimeter uses liquid argon as the active medium. Three cryostats contain the liquid argon separating the calorimeter in a central and two forward parts. This allows access to the central detectors within the calorimeter cavity. The central calorimeter (CC) covers the region $|\eta| < 1.0$, while the symmetric end calorimeters (EC) extend forward to $|\eta| < 4.0$. The number of nuclear absorption lengths (λ) for the CC (EC) is typically of 7 (9). Each cryostat is divided into an electromagnetic (EM), fine hadronic (FH), and a coarse hadronic (CH) section. The EM and FH sections contain uranium absorber plates, while the CH has copper or stainless steel absorber plates. Radially, from the inside out, the EM calorimeter with 4 absorber/readout layers is followed by the FH and CH sections with up to 4 layers.

The basic detection unit of the calorimeter is called a calorimeter cell, shown

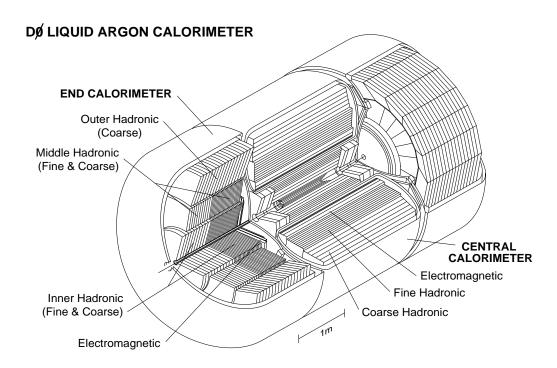


Figure 2.4: The DØ calorimeter consists of three modules (two end calorimeters and a central one). Each module is divided into an electromagnetic, fine hadronic, and coarse hadronic section.

in Figure 2.5. A cell consists of a grounded absorber plate and a signal board maintained at +2 kV. Ionization electrons drift to the readout boards where the collected charge is converted into a voltage signal. The typical cell size of $\Delta\phi \times \Delta\eta = 0.1 \times 0.1$ provides excellent shower position resolution, given that the common jet size is of $\sqrt{(\Delta\phi)^2 + (\Delta\eta)^2} = 0.5$. Table 2.1 summarizes the parameters of the central calorimeter, which is the only section relevant for this analysis.

One distinct characteristic of the DØ calorimeter is its pseudo-projective geometry. Straight lines can be drawn from the center of the detector through the centers of arrays of cells forming a calorimeter tower. The entire calorimeter is segmented into ~ 6000 towers. Figure 2.6 shows a projection of one quadrant of

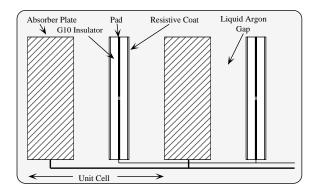


Figure 2.5: Schematic view of a calorimeter cell.

the DØ calorimeter in the y-z plane.

Inter-Cryostat Region (ICR)

The pseudo-rapidity region defined by $0.8 < |\eta| < 1.4$ suffers from depleted instrumentation because this volume is occupied by support structures, the cryostat walls and module end plates. To improve the sensibility in this region two systems were installed, the Intercryostat Detector and the Massless Gap detector. The Intercryostat Detector is a set of scintillation counters mounted on the front surface of the end calorimeters. The Massless Gaps are separate single cell structures installed between the central and end calorimeters cryostat walls.

Calorimeter Readout

The signals induced in the readout pads are pulses with widths of the order of 450 ns. The collected electrons are integrated producing a signal which peaks 2μ s after a $p\bar{p}$ bunch crossing. The decay time of this signal is 30μ s. Each cell is sampled twice, once at the time of bunch crossing (base) and again 2μ s later (peak). The difference between the two voltages is the raw energy of the cell, which can have negative values. The raw energy thus depends on previous crossings, because the

CC Module	EM	FH	CH
Rapidity Range	$ \eta < 1.2$	$ \eta < 1.0$	$ \eta < 0.6$
Absorbing Material	Uranium	Uranium	Copper
Absorber Plate Thickness	2.3 mm	2.3 mm	$46.5~\mathrm{mm}$
Total Depth (X_0)	20.5	96	32.9
Total Depth (λ)	0.76	3.2	3.2
Number of Layers	4	3	1
Depth per Layer	$2, 2, 7, 10 X_0$	$1.3, 1.0, 0.9 \lambda$	3.2λ
Segmentation	0.1×0.1	0.1×0.1	0.1×0.1
	$0.05 \times 0.05 \text{ (layer 3)}$		
Sampling Fraction	11.79%	6.79%	1.45%
Channels	10386	3000	1224

Table 2.1: Parameters for the central calorimeter.

signal decay is much longer than the accelerator bunch spacing $(3.5\mu s)$. This effect, which depends on luminosity and reduces the actual measured energy, is called pile-up. Another luminosity dependent cell energy offset contribution is generated by multiple interactions. Finally, the decay of radioactive uranium nuclei in the calorimeter results in an upward fluctuation in the measured cell's energies. This effect, uranium noise, does not depend on luminosity.

Calorimeter Performance

The thickness of the absorber plates and active regions between them is set to match the energy measured in hadrons showers to that of electromagnetic showers. The electron to pion response ratio of the DØ calorimeter, determined from test beam data, is of $e/\pi \sim 1.1$ at 10 GeV and falls to about 1.04 at 150 GeV. A value different from 1 causes deviation from linearity in the hadronic response

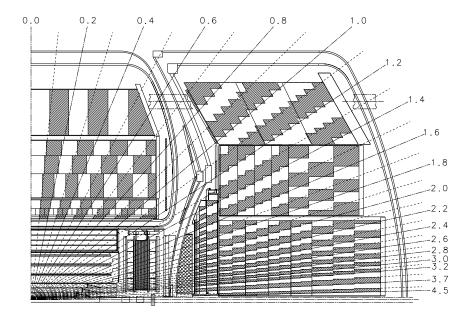


Figure 2.6: One quadrant of the DØ calorimeter and Central Detector, projected in the y-z plane. Radial lines indicate the pseudo-projective tower geometry. Each tower is of size $\Delta \eta \times \Delta \phi = 0.1 \times 0.1$.

versus energy, besides broadening the energy resolution and introducing tails in the energy distribution.

The fractional energy resolution, σ_E/E , is expected to improve as $1/\sqrt{E}$ because it is dominated by the statistical fluctuations in the number of sampled charged tracks, which is proportional to the incoming energy. Test beam studies show that the calorimeter energy resolution is approximately $15\%/\sqrt{E}$ for electrons and $50\%/\sqrt{E}$ for pions. The calorimeter energy resolution for jets is measured from collider data and will be discussed in chapter 6.

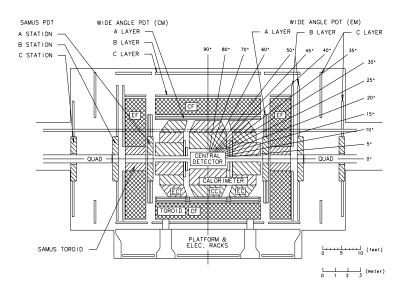


Figure 2.7: Elevation view of the DØ detector including the muon system.

2.2.3 The Muon System

The Muon system consists of three layers of proportional drift tubes (PDT) chambers which surround the calorimeter. The purpose of this system is the identification of muons produced in $p\bar{p}$ collisions and the determination of their trajectories and momenta. The innermost layer, the A layer, consists of four decks of PDT surrounded by toroidal magnets. The 2 Tesla iron toroids induce a bend in the moun trajectory. Two additional PDT layers, B and C, measure the moun direction after the bend, thus providing the moun momentum. The presence of a minimum ionization trace in the calorimeter can confirm the muon identification. The Muon System can be used in jet analyses to detect cosmic shower contamination and energy leakage outside the calorimeter.

2.2.4 The Level Ø Detector

The Level \emptyset system is designed to detect events containing an inelastic scattering and to provide a fast measurement of the location of the event vertex. It consists of two separate detectors, hodoscopes, located at each end of the central detector between the central and end calorimeters, approximately 140 cm from the

center of the detector. Each detector consists of two layers of rectangular scintillator bars, read out with photo-multipliers. An inelastic collision will typically include a large amount of activity in the far forward regions (from the spectator partons); thus, coincidence between the signals from the two scintillator arrays indicates the occurrence of a hard scattering. With very high efficiency these hodoscopes identify $p\bar{p}$ collisions, a prerequisite for most physics triggers (as described in chapter 3). By comparing the arrival times of the signals from the two arrays, the approximate position of the interaction vertex is obtained. The Level \emptyset system also provides a measure of the instantaneous luminosity by monitoring the interaction rate.

2.3 Detector Simulation

Detector simulation programs are widely used in high energy physics experiments. The DØ detector simulation program is based on the GEANT package [36]. The GEANT program describes the passage of elementary particles through matter. By specifying the detector volume and material the package allows the tracking of particles through the experimental setup simulating the detector response.

The full structure of supports and individual modules are present in the simulation of the calorimeters. The geometry and segmentation of the readout cells is imposed, the appropriate electron to hadron response is introduced and the sampling fluctuations and noise are accounted for. The electromagnetic showers evolve until the energy of the particles reach 200 MeV. Below this threshold, the energies are estimated from parametrizations. Since the full simulation of the $p\bar{p}$ interaction through the DØ detector is very time consuming, a "library" of particle showers has been developed [37]. These showers depend on a few particle parameters which allows to quickly simulate the interaction of a generated particle with the detector. The agreement between the shower library and the full

GEANT simulation is very good. In this analysis both types of simulated samples, "showerlibed" and full GEANT, have been used.

The combination of the event generators and detector simulation programs, is a critical aid to physics analyses providing a tool to understand the detector performance, and event reconstruction efficiencies.

Chapter 3

Data Collection and Event Reconstruction

This analysis is based on Run Ib data collected from December 1993 until July 1995. During this period of time there were 6 bunches of $\sim 150 \times 10^9$ protons and 6 bunches of $\sim 50 \times 10^9$ anti-protons rotating in opposite directions in the Tevatron and colliding every 3.5 μ s at the center of the DØ detector. Inelastic interactions were selected, and the recorded electronic signals sent to an array of digital logic circuits for further processing. Events which satisfy certain requirements were written to tape. The set of hardware and software event requirements is known as the trigger list. The interesting events which satisfy the trigger conditions were later processed offline. The following sections of this chapter describe the data collection process, the inclusive jet triggers used in this analysis and the offline event reconstruction.

3.1 Data Collection

Most of the bunch crossings are of little interest because they generally produce low transverse momentum objects. The DØ trigger system has to quickly select the interest events reducing the event rate to that at which events can be written to tape. There are three levels of decision making: Level 0, 1 and 2. Each subsequent level is more discriminating and time consuming. A block diagram of the three levels is shown in Figure 3.1.

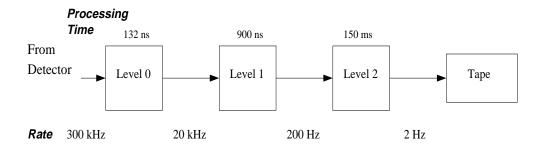


Figure 3.1: Block diagram of the DØ trigger system.

3.1.1 The Level Ø Trigger

The events of interest for the inclusive jet cross section measurement, and most of the analysis in collider experiments, are those resulting from a parton-parton scattering process, ie, inelastic proton-antiproton scattering. The ability to distinguish between elastic and inelastic events relies on the scintillation hodoscopes discussed in chapter 2. When a parton-parton scattering process occurs, the final state particles from spectators partons tend to have low-angle trajectories. Thus the Level \emptyset Trigger requires signals from both hodoscopes within a small period of time, which indicates that a $p\bar{p}$ inelastic collision has occurred. The hodoscopes provide a time resolution of about 100 ps which allows to signal inelastic collisions with nearly 100% efficiency. From the time of flight difference the Level \emptyset also provides the z position of the interaction vertex with a 3.5 cm resolution. The processing time of this trigger level is 132 ns.

The Level Ø Trigger reduces the event rate of 286 kHz to 20 kHz for a typical luminosity of $\mathcal{L} = 0.5 \times 10^{30} \text{ cm}^{-2} \text{ sec}^{-1}$. Selecting interesting events is the main

goal of the trigger system. It is also necessary to reduce the amount of data recorded by the experiment. The average size of the digitized detector information of a typical event is 500 kBytes, storing all the events that satisfy the Level Ø Trigger requires recording 10 GBytes per second. Further selection is necessary to reduce this information to a manageable level.

Zero and Minimum Bias Data

Not all data recorded by $D\emptyset$ is subjected to the Level \emptyset requirement. Diffractive events, in which one proton is elastically scattered, did not require a Level \emptyset trigger. More important for this analysis, some portion of the data was recorded with no Level \emptyset requirement, the so called *zero bias* data. This data is crucial to perform systematic studies related to the momentum calibration of jets. Also important is the *minimum bias* data, which only requires a Level \emptyset trigger. The relevance of these samples will be discussed in chapter 5.

3.1.2 The Level 1 Trigger

The Level 1 trigger system consists of hardware logic circuits which quickly filters the data steam, reducing the event rate from 20 kHz to 200 Hz. Events have to be selected within the $3.5\mu s$ window between beam crossings. Thus only the hit information from the calorimeter and the muon system are used in this stage. The muon triggers were not used in this analysis and are not discussed further. The calorimeter towers are grouped into 2×2 arrays $(0.2 \times 0.2 \text{ in } \eta - \phi \text{ space})$, called a trigger tower. The trigger tower transverse energy is calculated as the sum of the transverse energy of the included calorimeter towers. The energy of the electromagnetic portion of a trigger tower is used to make photon and electron triggers. Groups of 4×8 trigger towers defined the large tiles $(0.8 \times 1.6 \text{ in } \eta - \phi \text{ space})$. The energy of these tiles is, again, calculated as the sum of the transverse energy of the included trigger towers. An event passed the Level 1 requirements

if one or more trigger towers or tiles satisfied different requirements. For example a low energy jet trigger might require a trigger tower with at least 2 GeV while a high E_T jet trigger will require one tile above 45 GeV.

Using the Level \emptyset fast z vertex information the missing transverse energy of the event is calculated. Each cell in the calorimeter is given a four-vector, with an energy equal to the measured energy in the cell, a direction pointing from the interaction vertex to the center of the cell, and a mass of zero. The transverse components of these vectors are summed over all the calorimeter cells (including the ICD). The negation of this vector is then the missing transverse energy of the event. This information can also be included as part of the requirements a certain trigger has to fulfill.

Some triggers, which might have a relative low physics interest, are passed too often and saturate the next trigger level. In order to reduce the amount of data from these triggers only one out of a fixed number of passed events will actually pass the Level 1 trigger. Triggers with this additional restriction are said to be prescaled. The maximum number of triggers available at the Level 1 is 32. If one of these 32 trigger bits is true, the event is sent to the next trigger level.

3.1.3 The Level 2 Trigger

The Level 2 Trigger system consists of a large number VAX workstations working in parallel. The incoming events from the Level 1 trigger are reconstructed using the information of the entire DØ detector. Simplified algorithms are used to reconstruct the Level 2 physics objects, like electrons, muons and jets. The Level 2 Trigger system contains 128 sets of requirements, or trigger filters, which are associated to the different Level 1 trigger bits. For every incoming event the Level 2 framework checks the Level 1 trigger bits, gathers the digitized information from the different detectors and runs the corresponding filters. The event rate is thus reduced to 2 Hz. The typical size of a recorded event is of 500 kBytes. Similarly

to Level 1, the 128 Level 2 trigger bits can also be prescaled.

3.1.4 The Jet Triggers

This analysis uses the five inclusive jet triggers. The Level 1 jet triggers required at least one tile above a certain threshold. The centroid positions of all the Level 1 tiles are then passed to the Level 2. The Level 2 fast jet finding algorithm starts by finding the E_T weighted centroid of a 7×7 tower square around each E_T -ordered Level 1 tile. The E_T of all trigger towers, not already included in other Level 2 jet, within a radius of 0.7 in $\eta - \phi$ space of this centroid are summed up to obtain the Level 2 jet E_T . The Level 2 single jet filters required at least one Level 2 jet above a certain threshold. The five filters used in this analysis are: Jet_20, Jet_30, Jet_50, Jet_85, and Jet_115, where by convention, the number indicates the Level 2 E_T threshold in GeV. The lowest (highest) E_T jet trigger is also called Jet_Min (Jet_Max). The data collected with the Jet_Min trigger was only used to produce intermediate results and not the final cross section. Table 3.1 summarizes the Level 1 and Level 2 requirements the the inclusive jet triggers used in this analysis.

The inclusive jet cross section falls very steeply with p_T , thus the rate of a given trigger with a certain minimum p_T requirement can be many orders of magnitude larger than another trigger with a larger threshold. For this reason all triggers except Jet_Max were prescaled.

3.2 Offline Reconstruction

The raw event data which comes from the detector is given in terms of quantities such as digitized counts in a calorimeter cell, counts per time bin for a tracking chamber wire, and so on. However, these quantities in themselves are not very interesting. The patterns of ionization in the calorimeter and tracking chambers

Trigger Name	Run	Level 1 (GeV)	Level 2 (GeV)
	Number	- 1 tile with -	- 1 L2 jet with -
Jet_Min	all	$E_T > 3$	$E_T > 20$
Jet_30	all	$E_T > 15$	$E_T > 30$
	≤ 77824	$E_T > 35$	
Jet_50	$77825 \le \text{run} \le 85226$	$E_T > 25$	$E_T > 50$
	≥ 85227	$E_T > 15$	
Jet _ 85	$77824 \le$	$E_T > 60$	$E_T > 85$
	≥ 85227	$E_T > 35$	
	≤ 77824	$E_T > 60$	
Jet_Max	$77825 \le \text{run} \le 85226$	$E_T > 35$	$E_T > 115$
	≥ 85227	$E_T > 45$	

Table 3.1: Level 1 and Level 2 inclusive trigger configurations.

are presumably due to particles originating from a collision which interact within the detector; the kinematic parameters of these physical objects are needed. The process of turning the raw detector data into descriptions of objects such as leptons and jets is called reconstruction, and is carried out by a computer program.

When a quark or gluon leave the site of a hard scattering, it cannot remain free, but instead hadronizes, or fragments into a collection of colorless hadronic particles. These particles will typically lie around the direction of motion of the original parton, and will show up in the detector as a cluster of calorimeter cells.

The digitized signals of the calorimeter cells are converted to GeV according to test beam measurements, in which the response of calorimeter modules to beams of known energy was measured. The transverse energy of each cell is calculated using the position of the primary interaction vertex, as determined by the central tracking chambers. Cells with the same η and ϕ coordinates are summed together

in the electromagnetic and hadronic calorimeters to produce towers. These towers are the input to the jet clustering algorithm.

3.2.1 Determination of the Interaction Vertex

The precise determination of the interaction vertex coordinates is essential to obtain the transverse missing energy of the event and the E_T and η of the jets. The event vertex position is determined from the tracks reconstructed by the vertex chamber with a resolution of 50 μ m (0.65 – 0.95 cm) in the x-y (z) position, depending on the number of tracks and their angular distribution. The difference on the resolution of the vertex coordinates is caused by the fact that the wires of the vertex chambers are oriented along the beam direction thus providing better resolution in the transverse plane than in the z direction. In events with more than two reconstructed vertices, the vertex finding algorithm determines the interaction point from the candidate with more tracks [38].

3.2.2 Missing Transverse Energy

The missing transverse energy vector of an event is defined as:

$$\vec{E}_T = \left(\vec{E}_x \; ; \vec{E}_y \right) = \left(-\sum_{i}^{cells} E_{x,i} \; ; -\sum_{i}^{cells} E_{y,i}\right) \tag{3.1}$$

where the sums are aver all calorimeter cells including the Intercryostat Detectors and Massless Gaps. The missing transverse energy of an event (E_T) is the magnitude of E_T . In an ideal calorimeter, a non-zero missing transverse energy indicates the presence of non-interacting particles in the event, such a high p_T neutrino or muon. Neutrinos do not interact within the calorimeters while a high p_T muon behaves as minimum ionizing particles depositing only about 3 GeV of their energy. In a real calorimeter, the presence of E_T is also affected by electronic and uranium noise and the energy and position resolutions. In QCD events small values of E_T are expected.

3.2.3 Jet Reconstruction Algorithms

The k_{\perp} and cone jet algorithms were already described in section 1.3. However, limited computer processing time does not allow these algorithms to run on the ~ 6000 calorimeter towers of the DØ calorimeter. Preclustering algorithms are employed to reduce the number of inputs to the algorithms.

k_{\perp} Preclustering

The k_{\perp} algorithm is an $\mathcal{O}(n^3)$ algorithm (ie, for n input vectors, $\sim n^3$ calculations must be performed). In order to reduce the computer processing time required by the algorithm a preclustering procedure is used [39]. Towers are merged if they are close together in $\eta - \phi$ space, or if they have small transverse energy. Cells with $E_T < -500$ MeV are removed, cells with small negative energy are allowed, but cells with high negative E_T are spurious. Next the towers are sorted in $\eta - \phi$, starting at $\eta = -9$ and $\phi = 0$, the closest towers are combined into preclusters such that no two preclusters are within $\Delta R = \sqrt{\Delta \eta^2 + \Delta \phi^2} = 0.2$. The combined kinematic variables are calculated using the Snowmass prescription [14]:

$$E_{T} = E_{T,i} + E_{T,j}$$

$$\eta = \frac{E_{T,i} \ \eta_{i} + E_{T,j} \ \eta_{j}}{E_{T,i} + E_{T,j}}$$

$$\phi = \frac{E_{T,i} \ \phi_{i} + E_{T,j} \ \phi_{j}}{E_{T,i} + E_{T,j}}$$

The procedure continues in the ϕ direction and then it is iterated over increasing η . Finally, all preclusters with $E_T < 200$ MeV are redistributed to neighboring preclusters.

The 200 MeV cut was tuned to produce about 200 preclusters per event, to fit the processing restrictions. The preclustering parameters, $\Delta R = 0.2$ and $E_T < 200$ MeV, have no effect on the energy of the reconstricted jets (see appendix A). In order to perform consistent comparisons between the data and Monte Carlo simulations the preclustering algorithm is also applied in simulated events.

Cone Preclustering

In the cone jet algorithm case, calorimeter towers are first sorted in E_T , and a set of 'seed' clusters are formed. Starting with the highest- E_T tower which has not yet been assigned to a precluster, the precluster is formed from all contiguous towers out to a radius of 0.3 in $\eta - \phi$ space. Preclustering continues until all towers with $E_T > 1$ GeV have been assigned to a seed cluster. For each precluster, the E_T -weighted centroid defines the axis of the corresponding jet candidate.

k_{\perp} and Cone Jets Sample

The implementation of the k_{\perp} algorithm in the offline event reconstruction environment was done as part of the DØfix software package [40], which was not used for previous analysis based on the fixed cone algorithm. The DØfix program produced from the same data sample k_{\perp} (D=1) and cone (R=0.7) jets simultaneously.

A total of 31573 events were repeated in the DØ fixed data. These events were removed from the sample. Repeated events represented 1.5%, 1.7%, 1.5% and 2.2% of the cross section for Jet_30, Jet_50, Jet_85 and Jet_Max respectively.

The DØ fixed code introduced additional corrections which are not applied in any earlier version of the standard reconstruction program, DØRECO. One of these corrections changed the cryostat factors (see Table 3.2) which introduced a multiplicative correction to the calorimeter cell information which affected k_{\perp} jets as well as DØ fixed cone jets [41]. The possible effects of this correction were studied and determined to be unimportant [42]. The routine to fit secondary vertices was also changed in DØfix.

The modifications to the cryostat factors and the secondary vertex algorithm determined that the cone DØfixed data is not identical to the previous DØRECO outputs. But as it will be shown in chapter 8 the differences are small.

DØ fixed Cryostat Factors		
ECN	\mathbf{CC}	ECS
1.0609	1.0496	1.0478

Table 3.2: Cryostat factors applied to the energy in the calorimeter cryostats by the $D\emptyset$ fixed code (ECN north cryostat).

3.2.4 Calorimeter Cell Restoration

The number of calorimeter cells with spurious energies and unusually high hit frequencies, called "hot" cells, observed during Run Ia was high. For Run Ib the AIDA [43] (Anomalous Isolated Deposit Algorithm) cell suppressor was introduced. In each event, prior to jet finding, cells with $E_T > 10$ GeV and more than 20 times the average E_T of its first longitudinal neighbors, were suppressed by a factor of 10^{-9} . Unfortunately, AIDA damaged many good jets by removing good isolated cells, result from the natural fluctuations due to hadronization, shower development and calorimeter segmentation.

About 8% of the events had at least one suppressed cell ($\approx 2\%$ more than one cell). Figure 3.2 shows the distribution of the distance in $\eta - \phi$ space between the closest jet centroid and the AIDA cell,

$$\Delta R = \sqrt{(\phi^{jet} - \phi^{cell})^2 + (\eta^{jet} - \eta^{cell})^2}$$
(3.2)

The majority of the cells were removed from a very close vicinity of the jet centroid. Fortunately, the information of the suppressed cells was included in the DØ fixed reconstructed data. AIDA cells that were not "true" hot cells were restored to the jet if they were within $\Delta R < 1.0$ of the original jet direction and did not carry more than 50% of the original jet E_T . The f_{E_T} variable represents the amount of energy in the AIDA cell with respect to the jet and it is defined as:

$$f_{E_T} = E_T^{cell} / (E_T^{jet} + E_T^{cell})$$

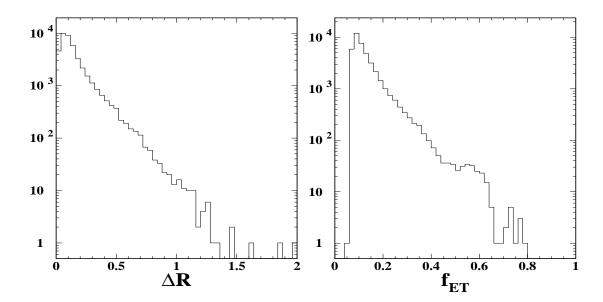


Figure 3.2: Left: The distribution of the distance between the AIDA cell and the jet centroid ($\Delta R = \sqrt{\Delta \phi^2 + \Delta \eta^2}$) for jets in the E_T range of 100 – 150 GeV for the central region. Right: the distribution of f_{E_T} .

Based on this distribution the cut of 0.5 (50%), which was used for cone jets [43], was also used for k_{\perp} jets.

The jet kinematic variables were recalculated following the k_{\perp} algorithm recombination scheme, the jet electromagnetic and coarse hadronic fractions were also recalculated, and finally the event missing transverse energy (E_T) was adjusted. The overall effect of the AIDA cell restoration procedure in the resultant cross section is small, about a 3% [42].

3.2.5 The H_T Correction

The tracking system reconstruction package often finds more than one vertex, and it may make a mistake in determining which of the vertices corresponds to the primary interaction. If more than one vertex is present then the two vertex candidates with the larger number of associated tracks are kept. Then

the event vertex is selected by choosing the reconstructed vertex which minimizes the magnitude of the vector sum of the jets E_T , this quantity is referred to as H_T . Since the reconstructed data does not have the information of the E_T for the second vertex, H_T is used instead for the events where the second vertex is selected. If the true primary vertex determined by this method is not the one found by the tracking system then all jet kinematic variables are recalculated using this new vertex position. This procedure lowers the cross section by about 4.5%.

Chapter 4

Data Selection and Associated Efficiency

In order to measure the inclusive jet cross section, jets that are produced in the hard interaction have to be identified and reconstructed by the k_{\perp} algorithm. QCD events are by far the most common result of the $p\bar{p}$ collision at DØ. Nevertheless there are a number of processes that can mimic the energy deposits left by "true" jets in the calorimeter. These "fake" jets are mostly caused by cosmic rays, losses of protons from the main ring into the detector¹, electrons or photons misidentified as jets, and electronic malfunctions. All of these processes may sometimes generate a large "fake" energy deposit in the calorimeter which may become a fake jet or it may be included as part of a good jet.

Event quality cuts, applied in an event-by-event basis, and jet quality cuts, applied in a jet-by-jet basis, were designed to remove the fake jets and events with fake energy deposits from the inclusive jet sample. The quality cuts are applied after running the cell restoration algorithm and the H_T correction. These cuts will occasionally remove a good event or jet, which has fluctuated outside the range set off by the quality cuts. To determine the inclusive jet cross section it is

¹The Main Ring pipeline runs through the calorimeter.

necessary to establish the efficiency of the cuts to compensate for the removal of good events or jets.

4.1 Cut Efficiency Calculation

Before describing the selection criteria, this section presents a general discussion on the determination of the selection cuts efficiencies. The first step is to obtain the "true" distribution of the variable being studied, *ie*, a distribution containing only good events or jets. Once this distribution is known, the cut in question is applied to this true sample, and the efficiency computed as:

$$\mathcal{E} = \frac{N_{pass}}{N_{tot}} \qquad N_{tot} = N_{pass} + N_{fail} \tag{4.1}$$

where N_{pass} and N_{fail} are the number of entries from the true sample that pass and fail the cut being studied and \mathcal{E} is its efficiency. By definition the variable N_{pass} is binomially distributed, therefore the variance of the efficiency is:

$$V(\mathcal{E}) = \frac{\mathcal{E}(1 - \mathcal{E})}{N_{tot}} \tag{4.2}$$

The systematic error involved in the determination of the cut efficiencies originates from the method used to obtain the true distributions. This contribution, which is added in quadrature to the binomial error, is estimated from the deviation of the original result from that based on a different method to obtain the true distribution. In the pseudo-rapidity region of this analysis the systematic contribution is almost negligible.

4.2 Event Selection

Events were selected by applying cuts on the missing transverse energy and on the position of the selected vertex.

4.2.1 The Vertex z Position Cut

The Z coordinate of the vertex was required to be within 50 cm of Z=0. This cut excludes events with jets which showered in the poorly instrumented intercryostat region and thus would degrade the resolution, and not events believed to be background. In addition, due to the pseudo-projective nature of the DØ detector, jet pseudorapidity is less precisely measured the further from the detector's center the vertex is found. Given that the primary vertex reconstruction efficiency does not depend on z, the efficiency of the vertex position cut (shown in Table 4.1) is calculated as the number of events that pass the cut divided the total number of events (Figure 4.1).

Filter Name	Vertex Cut Efficiency
JET_30	0.8918 ± 0.0004
JET_50	0.8936 ± 0.0006
JET_85	0.8968 ± 0.0004
JET_MAX	0.8927 ± 0.0006

Table 4.1: Vertex cut efficiency for each jet trigger.

4.2.2 The Missing Transverse Energy Cut

A cut based on the missing transverse energy of the event is introduced to remove cosmic showers and other unusual contamination that survives the standard jet cuts. This cut relies on momentum conservation, thus it can not be very strict since fluctuations in the jet energy deposits, due to resolution effects, cracks in the calorimeter, etc, may introduce high E_T to a good QCD event.

Instead of directly cutting on the $\not\!E_T$ of the event, the cut weights the missing transverse energy with that of the leading jet. The missing transverse energy

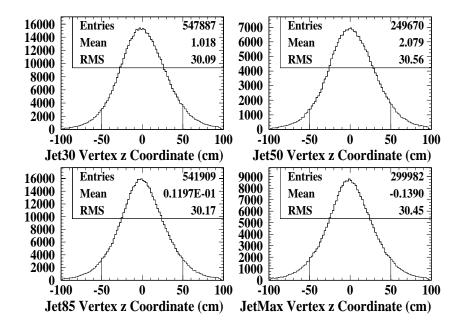


Figure 4.1: Distributions of the Z coordinate of the vertex position for the four jet triggers.

fraction of the event is defined as:

$$R_{MTE} = \frac{E_T^l}{E_T^{lj}} \tag{4.3}$$

where E_T is the missing transverse energy of the event and E_T^{lj} is the transverse energy of the leading jet, which was required to pass the jet quality cuts (see section 4.3). If the second vertex has been selected then the E_T is replaced by missing H_T (see section 3.2.5).

A typical distribution of R_{MTE} is shown in Figure 4.2. Following what was done in previous analyses using the fixed cone algorithm [15], events were rejected if the R_{MTE} exceeded 0.7. The E_T cut used for the central cone cross section [44] of $R_{MTE} < 0.3$ was not used because it removed good jets at high energies (see section 8.3). This cut was determined to be 99.8% efficient.

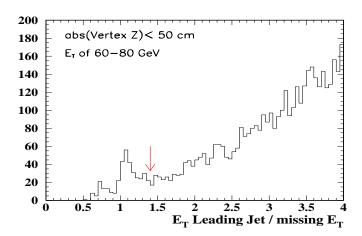


Figure 4.2: $1/R_{MTE}$ distribution for jets with p_T between 60 and 80 GeV. The vertical arrow shows where the cut is applied.

4.3 Jet Selection

QCD analyses use a number of "quality cuts" to discriminate between good and fake jet. These cuts are known as the standard jet quality cuts. This analysis makes use of these well studied [45] cuts to remove the fake jets from the inclusive k_{\perp} jet sample:

- The electromagnetic fraction of the total jet energy (EMF), *i.e.* the fraction of the transverse energy deposited in the electromagnetic modules of the calorimeter, was required to be between 5% and 95% in order to remove jets with noisy cells in the electromagnetic or hadronic calorimeter. It also effectively discriminates between hadronic and electromagnetic showers, though in any case, photon and electron production are not a background to worry about since their cross sections are orders of magnitude smaller than the jet cross section.
- The coarse hadronic fraction (CHF) cut required less than 40% of the total energy of the jet in the coarse hadronic layers of the calorimeter. This cut is designed to remove main ring contamination.

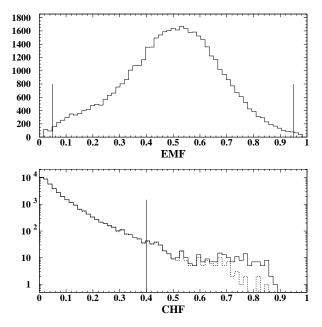


Figure 4.3: The EMF (top) and CHF (bottom) distribution of JET_50 jets of 100-120 GeV with only the vertex cut applied, the vertical lines indicate the low and high EMF cuts (top) and the CHF cut (bottom). The dashed line on the plot on the bottom is the CHF distribution after the R_{MTE} and EMF cuts.

The distributions of EMF and CHF are shown in Figure 4.3. To obtain the efficiency of the EMF cut, the "true" EMF distribution was inferred by applying restrictive z (|z| < 30 cm) and R_{MTE} ($R_{MTE} < 0.3$) cuts to the sample. Monte Carlo studies have shown that EMF distributions of good jets extend from EMF= 0 to EMF= 1 [45]. After the restrictive z and R_{MTE} cuts are applied, the same behavior is observed in the data. Thus the efficiency of this cut is the ratio of the number of jets with EMF $\in [0.05, 0.95]$ to the total number of jets. To estimate the efficiency of the coarse hadronic fraction cut a similar procedure is followed. The efficiency is again determined from the ratio of jets with CHF < 0.4 to the total number of jets.

The efficiency of the combined EMF and CHF cuts is shown in Figure 4.4 [46]. The errors were added in quadrature and then fit to a straight line.

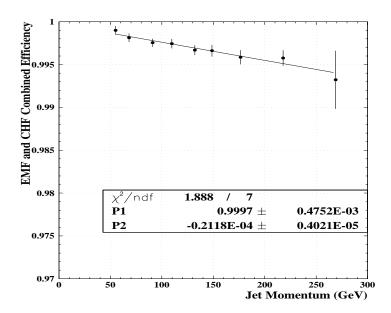


Figure 4.4: Combined efficiency of EMF and CHF cuts as a function of jet momentum.

Previous analyses based on the fixed cone algorithm included a third cut, the hot cell fraction (HCF) cut. The (HCF) is defined as the ratio of the transverse energies of the second most energetic cell in the jet to that of the most energetic one. This information was not included in the k_{\perp} ntuples. Fortunately this third cut is redundant and it does not affect the quality of the jets [45].

Chapter 5

Jet Momentum Calibration

The jet momentum measured by the DØ calorimeters is distorted by detector effects as well as by additional hadronic products resulting from the partons which do not participate in the hard scattering (the underlying event).

In order to obtain the momentum of the objects of interest before their interaction with the calorimeter, an average correction is applied, the scale correction, that restores the measured jet momentum to the final state particle level momentum. Hadronization effects are not taken into account in this correction, there is no intention to correct the measured jet momentum to the parton level. This is the most important correction of this analysis, in the sense that it has the largest effect on the result. Due to the steepness of the spectra (see section 7.2), a small change in the momentum of the jets causes a large change in the cross section. This correction is also the largest source of uncertainty in the inclusive jet cross section.

5.1 Momentum Scale Correction

The particle jet momentum is obtained by substracting the offset contribution to the calorimeter jet momentum and then dividing by the jet response. The offset part of the correction accounts for the momentum of the reconstructed jet not associated with the hard interaction itself: the uranium and electronic noise, pile-up from previous $p\bar{p}$ interactions, background from spectator partons and additional $p\bar{p}$ interactions. The response corrects for the calorimeter momentum response to jets and has little dependence on the jet algorithm.

Because the jet definition is given by the algorithm employed, the calibration will depend on the choice of the jet algorithm. Nevertheless some detector effects are independent of this choice. The k_{\perp} and cone scale corrections are very similar, in fact, the k_{\perp} momentum scale correction is based on the calibration of cone jets [47]; though the cone energy scale includes an additional factor which accounts for the fraction of the calorimeter shower not included inside the cone jet.

Given the measured jet momentum (p_{jet}^{meas}) , the corresponding particle level momentum (p_{jet}^{ptcl}) is given by the following relation, with \mathcal{L} being the instantaneous luminosity and η^{jet} and p_T^{jet} the jet pseudo-rapidity and transverse momentum respectively:

$$p_{jet}^{ptcl} = \frac{p_{jet}^{meas} - p_o(\eta^{jet}, p_T^{jet}, \mathcal{L})}{R_{jet}(\eta^{jet}, p_T^{jet})}$$

$$(5.1)$$

where p_o is the offset contribution from the underlying event and noise, and R_{jet} is the calorimeter response to jets. The offset correction is derived from studies of energy deposition patterns in minimum and zero bias events, while the response correction is measured using the missing E_T projection method.

After event reconstruction, the k_{\perp} jet momentum is corrected following equation 5.1. The calibration is implemented in the KTFIX module, part of the DØfix program, which also provides the associated errors.

5.1.1 Offset Correction

The offset correction removes from the reconstructed calorimeter jet the portion of the momentum which is not associated with the hard interaction. The total offset can be written as:

$$p_o = O_{ue} + O_{zb} \tag{5.2}$$

where O_{ue} is the offset from the underlying event and O_{zb} is the offset due to the overall detector environment. The source of the O_{zb} is the combined effect of the noise caused by the uranium radioactivity, pile-up and multiple interactions. The pile-up contribution to the offset is caused by the long shaping time of the calorimeter electronics, the drift time of the electrons in the calorimeter cells is about 450 ns, much shorter than the 3.5 μ s bunch crossing time. The O_{ue} and O_{zb} contributions are determined with a similar method, by overlaying data to Monte Carlo events. Monte Carlo samples of the $2 \rightarrow 2$ parton process were generated by HERWIG (version 5.9) [29] with the underlying event turned off. These samples are then processed through the GEANT [36] detector simulation package which provides a cell-level simulation of the calorimeter response and resolution. The digitized Monte Carlo events are then passed to the calorimeter reconstruction and jet finding packages, which defines the first sample of jets, the MC or Monte Carlo sample. The detector simulation does not include the effects of the uranium noise, nor the accelerator conditions causing multiple interactions and pile-up. The effect of these processes is modeled using zero bias events, which are random $p\bar{p}$ bunch crossing. The digitized calorimeter signals of these zero bias events are overlayed to the Monte Carlo digitized output and then passed through the reconstruction packages to produce a second jet sample, the ZB or zero bias sample. The two samples are compared on an event-by-event basis matching jets in the two samples which are close in $\eta - \phi$ space ($\Delta R < 0.5$). The O_{zb} offset contribution is then determined from the difference in the p_T of the matched jets. This contribution depends on the luminosity through the additional interactions and the pile-up contributions. Figure 5.1 shows the O_{zb} contribution as a function of jet pseudo-rapidity for different instantaneous luminosities.

The offset caused by the underlying event, O_{ue} , is determined using minimum

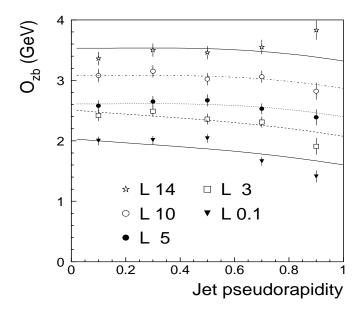


Figure 5.1: The offset O_{zb} contribution as a function of jet pseudo-rapidity for different instantaneous luminosities ($\mathcal{L} = 14, 10, 5, 3, 0.1 \times 10^{30} \text{ cm}^{-2} \text{ s}^{-1}$) indicated by the different symbol points. The curves are fits to the points at different \mathcal{L} , motivated by the functional form in [47]. The average correction for the central pseudo-rapidity region is about 2.6 GeV.

bias events, which require a hard scattering (see section 3.1.1). In addition to O_{ue} , minimum bias events include the effects of uranium noise, multiple interactions and pile-up. While the pile-up and multiple interactions contributions are luminosity dependent, the uranium noise and underlying event are not. The contributions of pile-up and multiple interactions are negligible at low luminosities, where only the effects of the underlying event and uranium noise are relevant. Zero bias events at low luminosity only contain the offset due to the uranium noise. Thus the O_{ue} is extracted from the p_T difference of matched jets in the minimum and zero bias samples at low luminosity. The O_{ue} contribution is shown in Figure 5.2 as a function of jet pseudo-rapidity, the average correction at central η is about 1.3 GeV.

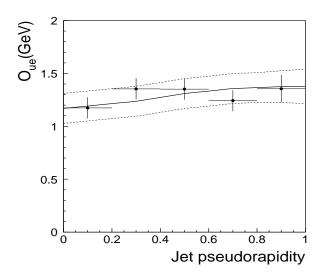


Figure 5.2: O_{ue} contribution as a function of jet pseudo-rapidity.

5.1.2 Jet Response

The calorimeter is calibrated from test beam data based on cell energy deposition for known incident particles assuming ideal instrumentation and linear response. However, in $p\bar{p}$ collision data, after reconstruction, the response may be less than unity due to non-linear response to low energy particles, uninstrumented regions of the detector and module-to-module response fluctuations. The calorimeter response to jets removes, in average, these effects.

Since Monte Carlo simulations do not mimic the jet momentum response and resolution to within uncertainties needed by this analysis [52], the jet momentum response measurement is derived from collider data, based on the p_T conservation in photon-jet (γ -jet) events [47]. The hadronic response is derived from the better understood electromagnetic response, using that in photon-jet events the transverse missing E_T should be zero. The photon momentum scale is determined from $Z \to e^+e^-$, J/ψ and π^0 data samples using the masses of these known particles.

In a two body γ -jet event, at particle level, the total missing transverse energy is zero:

$$\vec{p}_T^{\gamma} + \vec{p}_T^{particle\ jet} = 0 \tag{5.3}$$

However, the measured – calorimeter level – photon and jet transverse momenta may not balance:

$$\vec{p}_T^{\gamma} + R_{jet} \ \vec{p}_T^{particle \ jet} = -\vec{E}_T \tag{5.4}$$

where R_{jet} is the calorimeter response to jets ¹. Multiplying this equation by the unit vector \hat{n}_{γ} along the transverse direction of the photon and using that at particle level, $p_T^{\gamma} = -\hat{n}_{\gamma} \ \vec{p}_T^{particle\ jet}$:

$$R_{jet} = 1 + \frac{\hat{n}_{\gamma} \vec{E}_{T}}{p_{T}^{\gamma}} = 1 + MPF$$
 (5.5)

The missing E_T projection fraction (MPF) expresses the response in terms of well measured quantities. The jet response is expected to be momentum dependent. To avoid resolution and trigger biases which affect the measured jet momentum (p_{jet}^{meas}) , R_{jet} is binned in terms of $E' = \vec{p}_T^{\gamma} \cosh \eta_{jet}$, and then mapped onto p_{jet}^{meas} . Both \vec{p}_T^{γ} and η_{jet} are well measured quantities. R_{jet} and E' depend only on the jet position, which has little dependence on the jet algorithm. Figure 5.3 shows the calorimeter response to k_{\perp} jets as a function of p_{jet}^{meas} . Though the jet response as given by equation 5.5 does not depend on the jet algorithm, Figure 5.3 depends on the algorithm through p_{jet}^{meas} .

5.2 Width dependence of the Response

The MPF [47] method uses missing E_T (calculated as the vector sum of the transverse energies of all towers in the event) to infer the calorimeter response in the direction opposite to the photon. As stated above, the missing E_T is projected onto the photon direction for this purpose and the result divided by photon E_T . One plus this quantity (which is negative because the direction of the photon is opposite to that of the missing E_T) is what we call "the response of the calorimeter to the energy cluster centered around the direction opposite to the photon". This

 $[\]vec{p}_T^{calorimeter\ jet} = R_{jet}\ \vec{p}_T^{particle\ jet}$. The electromagnetic response is assumed to be one.

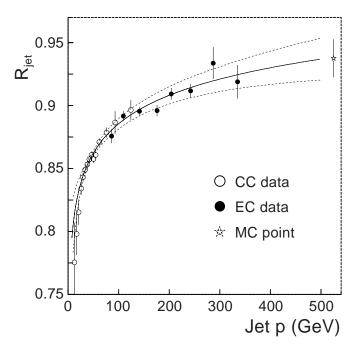


Figure 5.3: The calorimeter jet response (R_{jet}) for k_{\perp} jets with D=1.0 as a function of measured jet momentum. The functional form of the fit is $R_{jet}=a+b \ln p+c \ln^2 p$ (see [41]).

quantity is independent of the jet algorithm (no algorithm is used to calculate the MPF).

This method provides the right response for the recoil of the photon. The response to narrow hadronic energy clusters is better than the response to wide clusters of the same energy in the same calorimeter region. Previous studies [48] showed that the width of the recoil of the photon, of the sample used to derive the response using the MPF method, had the same average value than the jet object in the data sample. Though the width variable was calculated with towers inside the cone jet no difference is expected by using the k_{\perp} algorithm, because the response is a property of the energy cluster and does not depend on the difference in width calculated for the cluster using different algorithms.

5.3 Misclustering

The MPF method, through missing E_T , uses a vector sum E_T definition to determine the response. The cone algorithm assigns the scalar sum E_T of the towers to the jet's E_T . This produces a bias because MPF finds missing energy (lost by projecting the towers at the edge of the cone) which is not really missing from the scalar sum E_T used to derive the jet's E_T . There is not such a bias in the case of the k_{\perp} algorithm because it uses 4-vectors to determine the jet's p_T .

Although k_{\perp} jets are not affected by "showering losses outside the cone" they might be affected by "micslustered energy", energy incorrectly assigned to a jet at calorimeter level [48] (gained or lost). The effect would be minimal for an isolated jet, and gradually increases as other jets become closer in $\eta - \phi$ space. Misclustering might be included partially or totally by the MPF method |49|. A full Herwig-Geant Monte Carlo sample (plate level) was used to determine the magnitude of the effect. Figure 5.4 shows, for the first two leading matched $(\Delta R = \sqrt{\delta \eta^2 + \delta \phi^2} < 0.2)$ jets in the event, the ratio of calorimeter to particle jet p_T as a function of the closest jet (in $\eta - \phi$ space). All jets had to satisfy the standard quality cuts. A straight line was fitted to the points. From the plot one concludes that the leading jets loose energy to the other jets as these are closer in space. One also notes that, taking into account that the average distance between "good" jets in the data sample is $\Delta R \sim 1.6$ [42], the maximum effect is of the order of $\sim 1.5\%$ (that comes from the difference of the fit in Figure 5.4 at $\Delta R = 1.6$ and 3). The error assigned to the k_{\perp} momentum scale due to misclustering was 1% [48].

5.4 Monte Carlo Closure

To test the method used to determine the momentum correction a Monte Carlo sample can be used. The energy correction is derived from a Monte Carlo direct

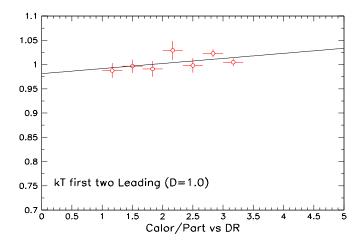


Figure 5.4: Misclustering effect studies. Ratio of calorimeter to particle jet p_T as a function of the distance to the closest jet (in $\eta - \phi$ space) from a plate level Monte Carlo sample. The points were fitted with a straight line, the fitted parameters being $m = 0.010 \pm 0.006$ and $b = 0.98 \pm 0.02$.

photon sample. k_{\perp} jets are reconstructed and their corrected momenta compared to the true values for the respective particle jets. Figure 5.5 shows that the calorimeter jets after the momentum correction agree well with the particle level jets. This is not a test of the offset because the Monte Carlo does not include uranium noise, multiple interactions and pile-up. This will be discussed further in section 8.4.1.

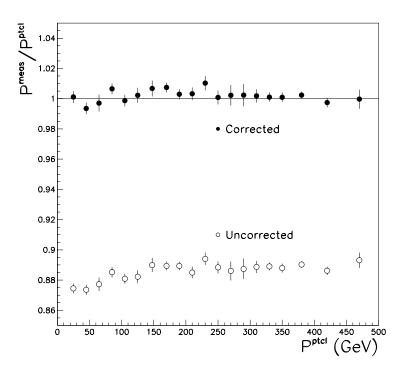


Figure 5.5: Monte Carlo closure test for k_{\perp} jets with D=1.0 in the central pseudo-rapidity region ($|\eta|<0.5$).

Chapter 6

Jet Momentum Resolutions

The inclusive jet cross section is measured as a function of the jet transverse momentum. As it will be shown on chapter 7, the finite momentum resolution of the detector distorts the observed cross section. In order to remove this effect it is necessary, in the first place, to determine the jet transverse momentum resolution as a function of p_T . This chapter presents the measurement of the k_{\perp} jet momentum resolution and discusses the differences between the k_{\perp} and cone jet cases.

6.1 Determination of the Jet Momentum Resolutions

The jet p_T resolution is measured for jets reconstructed with the k_{\perp} algorithm for $|\eta| < 0.5$ using di-jet events from collider data. The method was originally devised for the cone case [50, 15], and relies on the fact that both jets in a di-jet event should have equal transverse momenta, any difference between the measured values being attributable to the resolution of the detector.

The di-jet balance method used to determine the k_{\perp} jet momentum resolution relies on the asymmetry variable A, which is defined, for di-jet events, as the difference of the p_T of the two jets divided by the sum of the transverse momentum:

$$A = \frac{p_{T,1} - p_{T,2}}{p_{T,1} + p_{T,2}} \tag{6.1}$$

where $p_{T,1}$ and $p_{T,2}$ are the transverse momenta of the two jets. In the absence of any resolution effects, the two jets will have equal transverse momentum. Assuming that $p_{T,1}$ and $p_{T,1}$ have the same expectation values and variances, $E(p_{T,1}) = E(p_{T,2}) \equiv p_T \approx \frac{1}{2}(p_{T,1} + p_{T,2})$ and $Var(p_{T,1}) = Var(p_{T,2}) \equiv \sigma_{p_T}^2$, the fractional transverse momentum resolution is related to the variance of the asymmetry distribution by:

$$\frac{\sigma_{p_T}}{p_T} = \sqrt{2}\,\sigma_A\tag{6.2}$$

Thus by measuring the asymmetry distributions one can obtain the p_T resolution.

The dijet method, based on the conservation of transverse momentum, assumes there are only two jets in the event which have the same p_T . After the momentum scale correction is applied, di-jet events are selected by requiring a back-to-back cut of 5° to the two leading jets. Events are also required not to have a reconstructed third jet transverse momentum higher than 8 GeV (dijet cut). The three leading jets are required to pass the jet quality cuts (see section 4.3). The asymmetry distributions (see Figure 6.1) are fitted using a binned maximum likelihood technique, integrating the fitted gaussian function over the bin width [51]. Special care has to be taken to ensure that the trigger is fully efficient. Otherwise events in which the leading jet fluctuates high are favored, this generates a bump in the asymmetry distribution as shown in Figure 6.2.

The dijet asymmetry method does not return the correct fractional p_T resolutions. The two leading jets of an event may not balance due to extra jets in the event with $p_T < 8$ GeV (soft radiation), detector resolution, noise and underlying event fluctuations, algorithm effects and the particle imbalance contribution to the resolution. Most of these effects must be included in the resolution used to unsmear the jet p_T distributions, while others, like the soft radiation and the

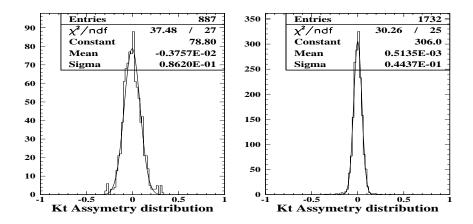


Figure 6.1: Asymmetry distributions, the p_T range of the plot on the left (right) is 40 - 47 GeV (106 - 113 GeV). The fits shown are gaussian.

particle jet imbalance contributions have to be removed. The two effects distort the p_T resolution estimated by the di-jet balance method. The soft radiation bias is caused by jets below the third jet soft radiation cut, which prevent the two leading jets from balancing in the transverse plane. Therefore, the measured resolutions are overestimates of the true resolutions. The second effect originates from the fact that at particle level, di-jets may not balance due to misclustering effects (incorrectly assigned, or not assigned, momentum to the jets). This contribution, referred to as the particle imbalance contribution, has to be removed. The following sections discuss these corrections.

The 8 GeV cut on the third jet was originally chosen in cone jet resolutions studies because clusters below 8 GeV were removed from the sample, although jets with energy below this value could result because of splitting and merging [52]. For all the events reconstructed using the k_{\perp} algorithm, there was always a reconstructed third jet (which is not the case with the cone algorithm). The minimum p_T of the jets is only limited by the 200 MeV cut applied in the pre-clustering procedure of the calorimeter cells. The fact that these lower energy jets are reconstructed allows a for better study of the soft radiation correction, discussed

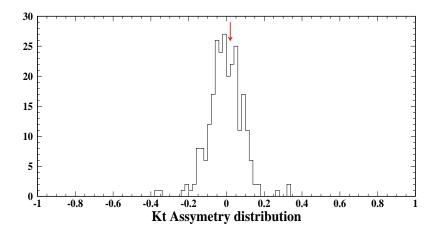


Figure 6.2: The asymmetry distribution for Jet_50 data with the p_T of the leading jet between 50 and 60 GeV. In order to remove the bump at the center of the distribution, the trigger has to be 100% efficient. Jet_50 was used above 100 GeV.

below.

6.1.1 Soft Radiation Correction

In order to evaluate and remove the bias caused by third jets below the di-jet cut, the resolutions were determined from samples with increasingly restrictive di-jet cuts, from 40 to 4 GeV. The results are then extrapolated to the ideal case in which the di-jet cut is zero.

For each asymmetry bin the following ratio is calculated:

$$\left(\frac{\sigma_{p_T}}{p_T}\right)^{Cut=\epsilon \,GeV} / \left(\frac{\sigma_{p_T}}{p_T}\right)^{Cut=8 \,GeV}$$
(6.3)

Each ratio is then fitted with a straight line and extrapolated to $\epsilon = 0$. Figure 6.3 shows the ratios for two p_T ranges, see [53] for a complete set of plots. Defining $K(p_T)$ as:

$$K(p_T) = \left(\frac{\sigma_{p_T}}{p_T}\right)^{Cut = 0 \, GeV} / \left(\frac{\sigma_{p_T}}{p_T}\right)^{Cut = 8 \, GeV}$$

$$(6.4)$$

the unbiased fractional E_T resolution is obtained from:

$$\left(\frac{\sigma_{p_T}}{p_T}\right) = K(p_T) \times \left(\frac{\sigma_{p_T}}{p_T}\right)^{Cut = 8 \, GeV}$$
(6.5)

The functional form for K is $K(p_T) = 1 - \exp(-\alpha - \beta p_T)$. Figure 6.4 shows the result for $K(p_T)$ as well as the best values for the parameters. As expected the size of the correction decreases as the transverse momentum increases.

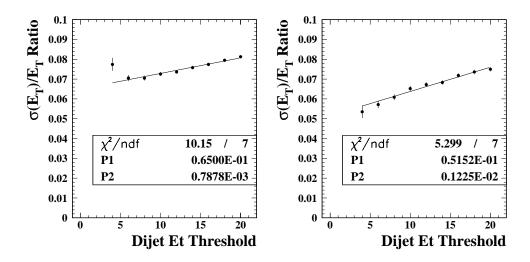


Figure 6.3: Resolution ratios versus dijet threshold. E_T range are 113 – 130 GeV (left) and 130 – 150 GeV (right).

The point-to-point correlations in the ratio plots are very large because each sample is a sub-sample of the previous one. A conservative uncertainty for $K(p_T)$, is obtained by adding in quadrature the error in the fit and the variation in the value obtained for K if only the last six thresholds (10, 12, 14, 16, 18 and 20 GeV) are used.

6.1.2 Particle Level Imbalance Subtraction

The contribution of the particle level imbalance can be estimated applying the dijet p_T balance method to Monte Carlo particle level events, after the soft radiation correction is applied. The result obtain for $(\sigma_{p_T}/p_T|^{pjet})_{asym}$ from a HERWIG

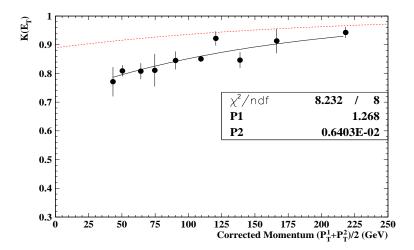


Figure 6.4: Soft radiation correction as a function of p_T . The dashed line is the cone result (see section 6.3.1). The fit is $K(p_T) = 1 - exp(-\alpha - \beta p_T)$ with $\alpha = 1.27 \pm 0.11$ and $\beta = 0.0064 \pm 0.0011$.

sample is shown in Figure 6.5 (along with the result for cone, which will be explained in section 6.3.1). The corrected fractional E_T resolutions is obtained from the expression:

$$\left(\frac{\sigma_{p_T}}{p_T}\right)^2 = \left(\frac{\sigma_{p_T}}{p_T}\right)_{asym}^2 - \left(\frac{\sigma_{p_T}}{p_T}|_{pjet}\right)_{asym}^2$$
(6.6)

where the suffix asym stands for the $K(p_T)$ corrected resolution.

6.1.3 k_{\perp} Resolutions

The resolutions for $|\eta| < 0.5$ are given in Table 6.1 and plotted in Figure. 6.6. The final p_T resolution is parameterized as:

$$\frac{\sigma_{p_T}}{p} = \sqrt{\frac{N^2}{p_T^2} + \frac{S^2}{p_T} + C^2} \tag{6.7}$$

which is a standard functional form. The first term, N, accounts for the noise contribution at low momentum, S is the sampling term (see section 2.2.2) and the constant term, C, is the resolution limit at high p_T . The band in Figure 6.6 is

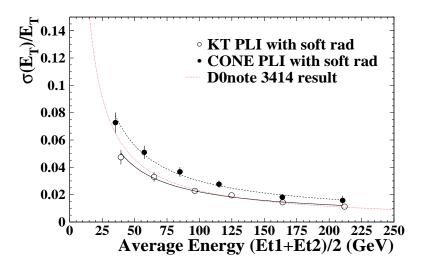


Figure 6.5: k_{\perp} particle imbalance contribution determined from a HERWIG Monte Carlo sample (open circles). The full circles are the particle imbalance contribution for cone jets, the dashed line is the result from [54].

the total systematic error, obtained by propagating the errors from the gaussian fits to the asymmetry distributions, the error in the determination of $K(E_T)$, the error of the particle imbalance substraction, and an additional 0.5% error. The later contribution accounts for the error in the asymmetry method estimated by the Monte Carlo closure test (see section 6.3.2). The error contribution and the correlation matrix can be found in [53].

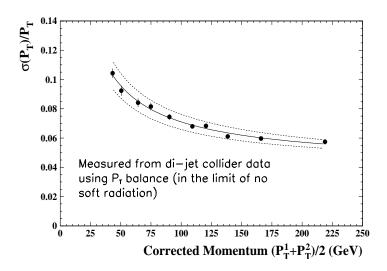


Figure 6.6: k_{\perp} Jet p_T fractional resolution for $|\eta| < 0.5$.

$(p_T^1 + p_T^2)/2$	Uncorrected	Soft Rad.	Part.	Corrected
(GeV)	Resolutions	Corr.	Corr.	Resolutions
43.3	0.133 ± 0.003	0.771	0.046	0.094 ± 0.003
50.4	0.115 ± 0.003	0.809	0.040	0.082 ± 0.003
64.3	0.099 ± 0.003	0.808	0.032	0.074 ± 0.003
74.8	0.093 ± 0.003	0.811	0.028	0.072 ± 0.003
90.3	0.082 ± 0.002	0.845	0.024	0.064 ± 0.002
109.3	0.071 ± 0.001	0.851	0.020	0.058 ± 0.001
120.5	0.070 ± 0.001	0.922	0.019	0.058 ± 0.001
138.4	0.061 ± 0.001	0.846	0.017	0.051 ± 0.001
166.0	0.057 ± 0.001	0.913	0.014	0.050 ± 0.001
218.9	0.052 ± 0.002	0.943	0.012	0.047 ± 0.002

Table 6.1: Measured resolutions for $|\eta|<0.5$

6.2 Monte Carlo Closure Test

The accuracy of the asymmetry based single jet resolution measurement can be determined using HERWIG Monte Carlo events. These include particle and calorimeter level simulation, allowing a direct comparison between particle jets and calorimeter jets. The calorimeter jets are matched to the particle jets and the variance of the ratio between their transverse energies is taken as the "straight" resolution (E_T^{cal}/E_T^{part}) . The asymmetry method is then applied, using only calorimeter jets. A comparison between both results is a test of the asymmetry method to within its uncertainty.

Each of the first two leading particle jets are matched to one of the two leading calorimeter jets, whichever is closer in the $\eta - \phi$ space, if the condition, $\Delta R = \sqrt{\Delta \eta^2 + \Delta \phi^2} < 0.2$, is satisfied. The cut of 0.2 is chosen because it accommodates both poor resolution low p_T jets and good resolution high p_T jets [51]. The distributions of E_T^{cal}/E_T^{part} are centered on one after applying the Monte Carlo k_\perp momentum scale correction.

The soft radiation and particle imbalance corrected asymmetry derived resolution is in good agreement, within errors, with the straight resolution, see Figure 6.7. Also included in the plot is a straight line fit to the points. A conservative error of 0.5% for systematic errors due to the measurement method is assigned.

6.3 Consistency Checks

6.3.1 Cone Consistency Check

As a cross check of the results obtained for the k_{\perp} algorithm, the resolutions for jets reconstructed using the cone algorithm were calculated using the k_{\perp} DØfixed data sample, which also contain cone jet information. Figure 6.8 shows the soft radiation correction for cone jets measured from the DØfixed sample. The energy

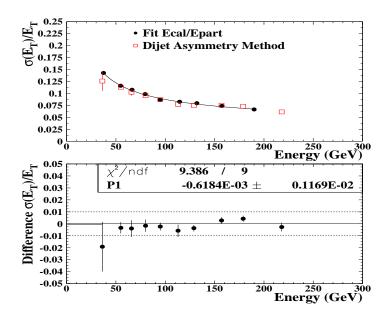


Figure 6.7: Comparison between resolutions obtained with the asymmetry and the straight resolution methods using a Monte Carlo sample.

of the cone jets was corrected using CAFIX5.2 [48]. Figure 6.9 shows the excellent agreement between the result using the cone jets from the k_{\perp} data sample and the one from reference [45], using the same particle imbalance contribution.

The particle imbalance contribution has also been recalculated using the cone information of the HERWIG k_{\perp} samples. The result obtained is 0.3-0.4% above the one used in reference [51]. Since the particle imbalance contribution, which is about two and a half times smaller than the uncorrected result, gets subtracted in quadrature (see section 6.1.2), a small difference of 0.3% is immaterial. Thus, the cone (R = 0.7) resolutions for the central region $(|\eta| < 0.5)$ using the k_{\perp} data sample are in very good agreement with previous results [45, 51].

6.3.2 Cross Checks of the Monte Carlo Closure Test

The Monte Carlo closure test was also done using the cone jets of the k_{\perp} HERWIG sample. The response and offset correction as detailed in [48] were applied to the

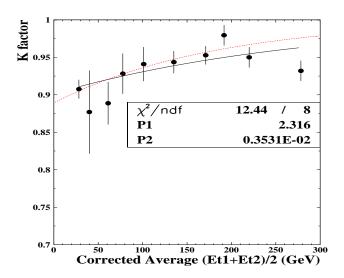


Figure 6.8: The soft radiation correction, $K(E_T)$, as a function of E_T for cone jets with R = 0.7 and in the central region ($|\eta| < 0.5$). The dashed line is the result in reference [51].

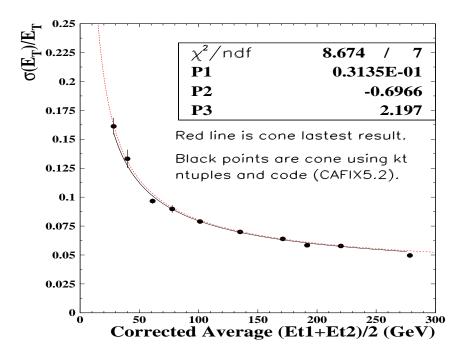


Figure 6.9: Cone consistency check, the back points are the result obtained in this analysis and the dashed line is the result from reference [51].

jets. After these corrections the distributions of E_T^{cal}/E_T^{part} were not centered in one, but off by $3\%^1$. A correction factor was applied to the sample to center the distributions in one.

The E_T^{cal}/E_T^{part} ratio is in good agreement with the resolutions calculated using the asymmetry method. This result is consistent with previous ones [51].

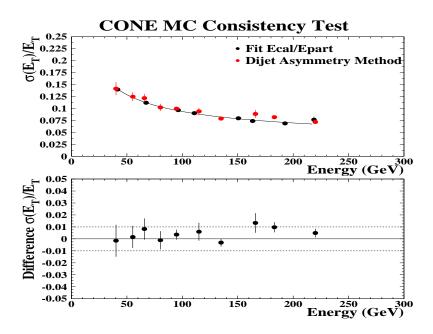


Figure 6.10: Cone Monte Carlo closure test.

6.3.3 Plate Level k_{\perp} and Cone Straight Resolutions

As another check of the results, the straight resolutions were extracted using a full HERWIG-GEANT Monte Carlo sample (plate level) for both k_{\perp} and cone jets. This is the best Monte Carlo sample, in the sense that it most closely simulates the data. Calorimeter jets were matched to particle jets as done in the case of showerlibed Monte Carlo, see section 6.3.2.

The distributions of E_T^{cal}/E_T^{part} were not centered on one, and, because there is no energy (or momentum) scale correction for either k_{\perp} nor cone plate level Monte

¹Because the momentum correction applied to the Monte Carlo jets was not compleate.

Carlo jets, an ad hoc correction was applied to the calorimeter jets, 6% for k_{\perp} and 7% for cone, which centered the distributions in one.

The sample available only allowed for one energy bin to be studied, 60 - 90 GeV, see Figure 6.11. The top plot is the straight resolutions for k_{\perp} (D = 1) and the bottom one is for cone (R = 0.7). Though the k_{\perp} straight resolution is 4% below the cone one, the error bands overlap and the result is consistent with the experimental measurement and with the closure tests.

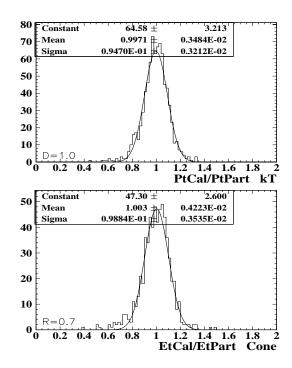


Figure 6.11: The straight resolutions from a plate level Monte Carlo sample. Top: k_{\perp} , 60 GeV (left) and 80 GeV bins. Bottom: cone 60 GeV (left) and 80 GeV bins.

6.3.4 Comparison between k_{\perp} and Cone resolutions

Uncorrected fractional resolutions

Figure 6.12 shows the comparison of the uncorrected fractional resolutions with a third jet cut of 8 GeV. Before doing any corrections the resolutions for k_{\perp} jets (D=1.0) are about 0.01 (in absolute value) below the resolutions for cone jets (R=0.7) as shown by the difference between the fits, see bottom of Figure 6.12.

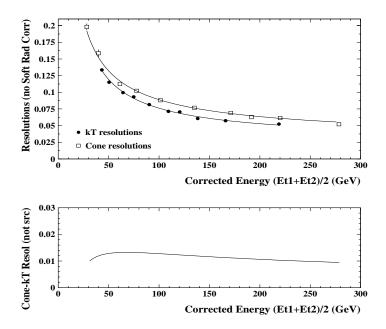


Figure 6.12: k_{\perp} and cone raw asymmetry comparison (third jet cut of 8 GeV). The bottom plot shows the absolute difference between the two.

Soft Radiation Correction

The soft radiation correction is larger for k_{\perp} jets, specially at lower energies. This could be caused by the inefficiency of the cone algorithm to reconstruct low energy jets [52]. Figure 6.13 shows the ratio of the soft radiation corrections for k_{\perp} and cone.

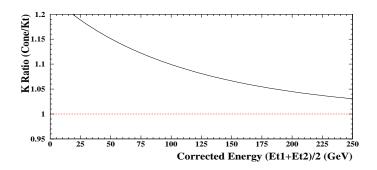


Figure 6.13: Ratio of the nominal soft radiation correction for cone and k_{\perp} jets.

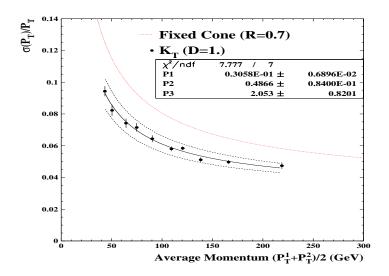


Figure 6.14: Cone and k_{\perp} jet fractional resolution for $|\eta| < 0.5$.

Final Resolutions Comparison

Figure 6.14 shows the nominal result for the cone resolutions [45] and the k_{\perp} result, Figure 6.15 shows the absolute difference between the k_{\perp} and cone fits. At low energies the difference is dominated by the different soft radiation corrections while at medium and high energies the intrinsic difference in the uncorrected fractional resolutions account for the result.

k_{\perp} and Cone Resolutions with Matched Jets

In an effort to understand the differences between the k_{\perp} and cone results, the resolutions for both algorithms were studied using matched jets (cone to k_{\perp}).

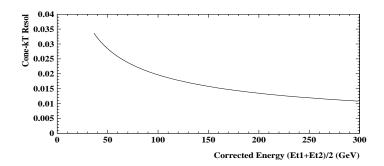


Figure 6.15: Difference of the nominal fits to k_{\perp} and cone resolutions.

The asymmetry distributions were fitted with a gaussian in this study. Only the events which satisfy the following criteria were used:

- 1. Events had to satisfied selection criteria (see chapter 4).
- 2. Same vertex for cone and k_{\perp} .
- 3. No AIDA cells in the event.
- 4. Cone and k_{\perp} jets have to pass the back-to-back and dijet cuts.
- 5. Match cone to k_{\perp} jets ($\Delta R < 0.5$, two leading jets).

The asymmetry distributions were filled with the most restrictive trigger cuts. Figure 6.16 shows the ΔR distribution between the leading two cone and k_{\perp} jets. Only matches with $\Delta R < 0.5$ were used.

Figure 6.17 shows the widths of the asymmetry distributions for both cone and k_{\perp} with matched jets and a dijet cut of 8 GeV. There is no significant difference between the two uncorrected resolutions. Below 90 GeV the statistics is poor, but above this energy both results are below the dashed line that is the latest fully corrected result for cone [45]. The soft radiation correction and the particle imbalance subtraction would further decrease the results.

One could explain the different results between matched and not matched cone jet resolutions if the soft radiation is underestimated in the cone case because the

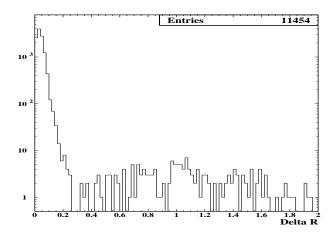


Figure 6.16: ΔR between the leading two cone jets and the matched k_{\perp} jets.

cone algorithm does not reconstruct low energy jets. This is not the case for the k_{\perp} algorithm. Figure 6.18 shows the E_T distribution of k_{\perp} jets above the cut of 8 GeV for events that passed the dijet cut for cone. Of the 19338 events that pass the cone quality, back-to-back and dijet (of 8 GeV) cuts, 5760 have a third k_{\perp} jet above 8 GeV, which the cone algorithm presumably failed to reconstruct. After matching the jets and applying the back-to-back and dijet cut to the k_{\perp} jets, the events with soft radiation that were not reconstructed by the cone algorithm are removed, selecting events where the two leading cone jets are better balanced. If no matching is done between k_{\perp} and cone jets then the cone jets yield a larger resolution as shown in Figure 6.6. However these results should be taken with care as the matching of jets can introduce biases (for example towards more narrow jets).

6.4 Conclusions

In this chapter, the determination of the k_{\perp} jet momentum resolutions has been described in detail. Closure of the method to derive the resolutions was obtained using a Monte Carlo sample, and from this closure a 0.5% systematic error was added to the other uncertainties. As a cross check to the k_{\perp} resolutions, the

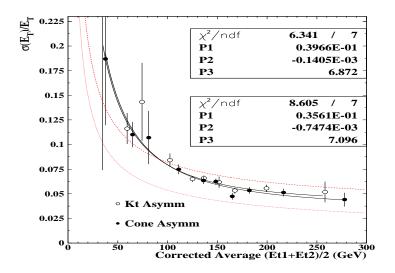


Figure 6.17: Uncorrected resolution using matched k_{\perp} (open circles and upper box) and cone jets with a dijet cut of 8 GeV. The bottom dotted line is k_{\perp} corrected result (soft radiation and particle imbalance corrections applied), the dashed line is cone's final result [45].

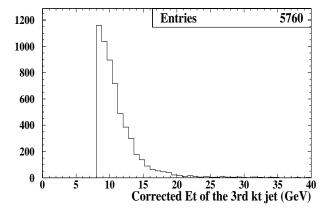


Figure 6.18: Transverse momentum of the third k_{\perp} jet for events without a third cone jet with E_T above 8 GeV.

cone jet resolutions were calculated from the DØfixed data. The DØfixed cone resolutions were in excellent agreement with previous (non DØfixed) results. The closure test of the dijet balance method for the DØfixed cone sample was also in agreement with the previous result. The difference between the k_{\perp} and cone resolutions may be explained because k_{\perp} jets are expected to be less sensitive to showering fluctuations, and the fact that the k_{\perp} algorithm reconstructs low energy jets more efficiently.

Chapter 7

The Inclusive Cross Section

The double differential jet cross section with respect to jet pseudo-rapidity and transverse momentum is defined by $d^2\sigma/(dp_T-d\eta)$. After the momentum scale correction, the experimental measurement of the single inclusive jet cross section, binned in terms of p_T and η , is determined as:

$$\left\langle \frac{d^2\sigma}{dp_T \ d\eta} \right\rangle (p\overline{p} \ \to jet + X) = \frac{N}{\Delta p_T \ \Delta \eta \, \mathcal{E} \, L}$$
 (7.1)

where the brackets indicate an average over the p_T and η bins, N the number of accepted jets in this bin, Δp_T and $\Delta \eta$ are the bin sizes and \mathcal{E} is the total efficiency in this bin. L is the integrated luminosity which sets the normalization of the measurement.

This chapter presents the results for the cross section measurement. The luminosity determination is discussed first, followed by the observed cross section. The effect of the finite momentum resolution on the observed cross section needs to be removed, this is done by the "unsmearing" procedure described in section 7.3. The final inclusive jet cross section is presented in section 7.4 together with the error matrix of the measurement.

7.1 Luminosity Determination

The instantaneous luminosity is the number of $p\bar{p}$ crossings per unit time and unit area. The integrated luminosity of a certain period of time is obtained by summing the instantaneous luminosities over the given period. The luminosity is obtained by measuring the rate of non-diffractive inelastic collisions [55]. This rate is measured by the Level \emptyset detector and corrected by its acceptance, multiple interaction events and beam halo.

The luminosity is measured for each individual trigger to account for different prescales and dead times. The integrated luminosity for the four triggers used in this analysis as taken from the Production Data Base is listed in Table 7.1. The luminosities for the k_{\perp} inclusive cross section are not the same to the ones used in the previous run Ib cone cross section analyses [15] because, as the k_{\perp} data was process through DØfix, the runs used are not the same. For a detailed list of the runs used in this analysis refer to [56].

Trigger Name	$\mathbf{Lum} \ (\mathbf{pb}^{-1})$
Jet_30	0.362
Jet_50	4.86
Jet_85	51.5
Jet_Max	87.6

Table 7.1: Trigger luminosities for the run Ib runs used in the k_{\perp} inclusive cross section analysis as extracted from the Production Data Base.

Due to discrepancies observed among trigger versions the luminosities for triggers Jet_30 and Jet_50 are poorly determined. These luminosities were established by matching the p_T spectrum associated with each trigger as described in section 7.1.2. First, however, it is necessary to determine the trigger thresholds, ie, the transverse momentum in which each trigger becomes fully efficient.

7.1.1 Trigger Thresholds

In order to determine the transverse momentum where each trigger becomes fully efficient, the ratio of two of the p_T corrected trigger cross sections is measured, requiring all the events to pass the less restrictive trigger (ie, for Jet_85/Jet_50 events are required to pass Jet_50). This ratio should approach unity if the less restrictive trigger sample is a complete subset of the more restrictive one when both are fully efficient. If this is not the case, the ratio will approach some arbitrary value given by the relative prescales of the two triggers. Figure 7.1 shows the "turn ons" for triggers Jet_30 , Jet_50 , Jet_85 , and Jet_Max (Jet_Min was used for the turn on of Jet_30), the transverse momentum at which each trigger is fully efficient is tabulated in Table 7.2.

Trigger Name	Fully Efficient at	
Jet_30	$60~{ m GeV}$	
Jet_50	$100 \mathrm{GeV}$	
Jet_85	$150~{ m GeV}$	
Jet_Max	$200~{ m GeV}$	

Table 7.2: Jet trigger thresholds.

7.1.2 Trigger Matching

The luminosities of the two highest jet triggers, Jet_85 and Jet_Max, were extracted from the production database based on the run number information. Unfortunately, since there is no information for the DØfixed streams in the production database, it is not possible to obtain the errors on the luminosities accurately [57], thus a conservative error of 8% is assigned to each trigger luminosity.

As mentioned before, the luminosities for Jet_30 and Jet_50 were not available for technical reasons, and had to be indirectly inferred by matching their

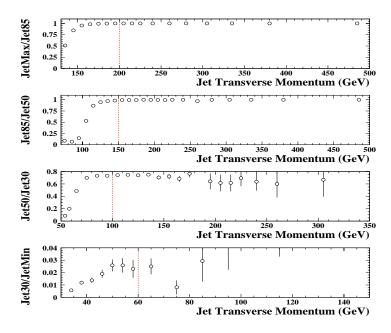


Figure 7.1: Triggers turn on.

 p_T spectrum to that of a higher energy trigger with well measured luminosity in the region where the latter is fully efficient. Jet_50 was matched to Jet_85 above 150 GeV, and then Jet_30 to the already corrected Jet_50, above 110 GeV. The overlap region of the two consecutive triggers is fitted with a constant, as shown in Figure 7.2, from which the corrected luminosity is calculated. Table 7.3 list the corrected luminosities for each trigger and the associated errors. The matching procedure introduces an additional uncertainty to the lower triggers.

Trigger Name	Luminosity	Error
	(pb^{-1})	(%)
JET_30	0.332	9.8
JET_50	4.36	9.3
JET_85	51.5	8
JET_MAX	87.6	8

Table 7.3: Trigger luminosities.

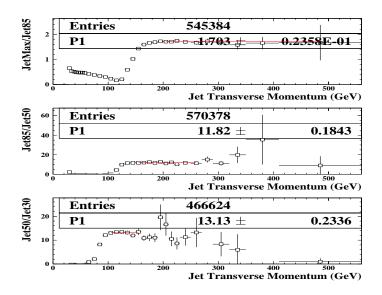


Figure 7.2: Ratio of trigger cross sections, from Top to bottom: Jet_Max/Jet_85, Jet_85/Jet_50 and Jet_50/Jet_30.

7.2 The Observed Inclusive Jet Cross Section

Following equation 7.1, a cross section is measured for each of the four inclusive jet triggers (see Section 3.1.4) and the results are combined such that each trigger is used as soon as it becomes fully efficient. The observed cross section for the central pseudo-rapidity region ($|\eta| < 0.5$) is presented in Figure 7.3. The number of jets in each p_T bin is Poisson distributed, thus the statistical errors are given by $\sqrt{N}/(\Delta P_T \Delta \eta \mathcal{E} L)$. The p_T binning was chosen following previous analyses based on the cone algorithm [15] to facilitate future comparisons.

The observed cross section is still distorted by the finite resolution of the detector. Earlier studies have determined that the effect of η resolution causes negligible changes in the central rapidity region cross section [45, 52] while distortions introduced by the finite calorimeter resolution on the jet momentum have to be removed.

Though the momentum mismeasurement due to the detector resolution is basically symmetric, in the sense that the jet momentum will fluctuate low or high

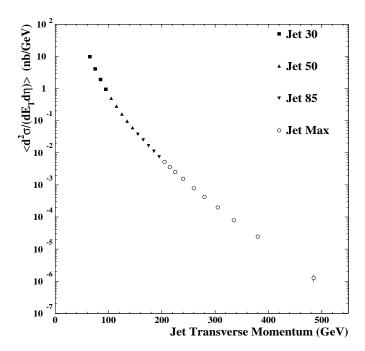


Figure 7.3: Observed inclusive jet cross section in the central pseudo-rapidity region. Errors are statistical only.

with the same probability (because of the hermeticity and linearity of the DØ calorimeters), a systematic shift to the cross section is introduced. This "smearing" effect results from the steeply falling nature of the p_T spectrum, as illustrated in Figure 7.4. For a given p_T bin, the p_T of the jets may fluctuate to a lower or higher bin. But as a result of the steepness of the spectrum more jets will fluctuate from a bin in the left to a bin to the right than the other way around, thus the effect of the p_T resolution is the inflation of the cross section. The jet p_T resolution measurement was presented in chapter 6, the following section discusses how the smearing effect is removed from the observed cross section.

7.3 Unfolding of the Cross Section

The DØ "unsmearing" or "unfolding" procedure [52, 44] is applied to the cross section in order to remove the upward smearing effect, caused by the finite mo-

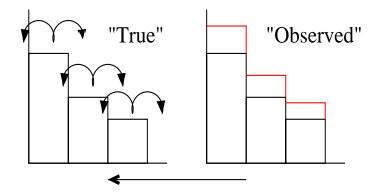


Figure 7.4: The finite momentum resolution of the detector inflates the observed cross section.

mentum resolution. A hypothetical unsmeared cross section is assumed, described by an ansatz function. This function is smeared with a gaussian of width equal to the measured p_T resolutions (see chapter 6) and the smeared result is compared with the observed cross section. The convolution of the trial ansatz function and the gaussian which yields the observed cross section can be written as:

$$f(p_T) = \int F(p_T') \frac{1}{\sqrt{2\pi}\sigma(p_T')} e^{-\frac{1}{2} \left(\frac{p_T - p_T'}{\sigma(p_T')}\right)^2} dp_T'$$
 (7.2)

where F is the ansatz function and f is the "smeared hypothesis", which should describe the observed data well. The functional form of the ansatz F is:

$$F(p_T, A, B, C) = e^A p_T^B \left(1 - \frac{2 p_T}{\sqrt{s}} \right)^C$$
 (7.3)

where A, B and C are the free parameters. To unsmear, the parameters of the ansatz are varied until the difference between the smeared hypothesis and the observed data is minimized. The data is then corrected by multiplying, in each bin, the observed cross section by the ratio of the unsmeared to smeared fitted ansatz functions. This ratio is called the correction factor:

$$C_{factor} = \frac{F(p_T)}{f(p_T)} \tag{7.4}$$

Figure 7.5 shows the unfolding correction factor as a function of jet p_T . The two outer solid curves show the error on the nominal correction due to the resolution uncertainties. This error was derived from the data by unfolding with the upper and lower estimates of the resolution curves. The correction is large at low p_T because of the steepness of the inclusive spectra, while at high p_T the correction increases due to the worse absolute p_T resolution. Table 7.4 includes the final ansatz parameter values together with the error matrix of the fit. The obtained value of the χ^2/ndf was of 27.7/24.

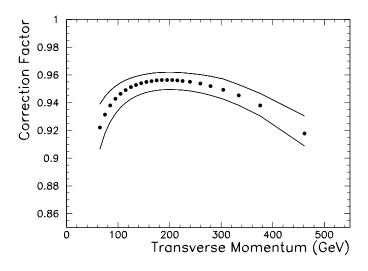


Figure 7.5: Unfolding correction factor as a function of jet p_T .

Parameter	Value	Error Matrix		
A	38.75	7.45×10^{-3}	1.93×10^{-3}	1.11×10^{-2}
В	-5.32	1.93×10^{-3}	5.00×10^{-4}	2.93×10^{-3}
C	7.46	1.11×10^{-2}	2.93×10^{-3}	1.85×10^{-2}

Table 7.4: Unsmearing parameters and errors.

In order to check the validity of the ansatz function used to unsmear the data,

two additional different functional forms have been tested:

$$F_1 = e^A p_T^B \left(1 - \frac{2 D p_T}{\sqrt{s}} \right)^C \tag{7.5}$$

$$F_2 = e^A p_T^B \tag{7.6}$$

Figure 7.6 shows the ratios between the unfolding correction factors using the "nominal" ansatz and functions F_1 and F_2 . In the first case there in no significant change in any bin but the last one (which has large uncertainties) where the effect is of the order of 3%. In the extreme case of F_2 the differences ranges from 3% for the first bin to 4% for the last one. Thus the "nominal" ansatz function was determined to be adequate.

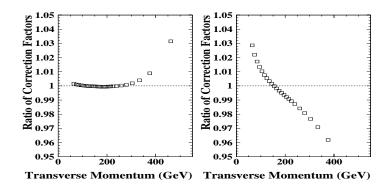


Figure 7.6: Effect of changing the ansatz function used to unsmear the data. The left plot corresponds to F/F_1 and the right on to F/F_2 (see text).

7.4 Final Inclusive k_{\perp} Jet Cross Section

The inclusive cross section for the central pseudo-rapidity region ($|\eta| < 0.5$) using the k_{\perp} algorithm at $\sqrt{s} = 1.8$ TeV is shown in Figure 7.7. It is obtained from the observed cross section after the bin-by-bin unfolding correction is applied. The errors on the points are statistical only. Table 7.5 lists the cross section, data errors and p_T bins. The included sources of systematic errors are jet and event selection, unsmearing, luminosity and the jet momentum scale, which is the

dominant contribution over the whole p_T range. The data points are plotted and tabulated at the p_T value where the function that best describes the cross section (see section 7.3) is equal to the average integrated cross section in the bin [58].

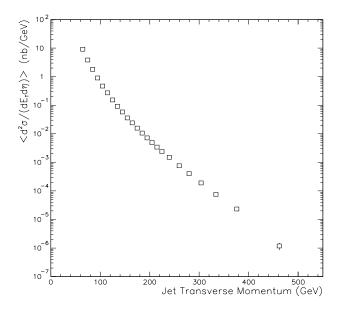


Figure 7.7: The central inclusive jet cross section with the k_{\perp} Algorithm. Only statistical errors included.

7.4.1 Relative Importance of the Corrections

The efficiency correction, the unsmearing procedure and the jet momentum calibration have different impacts on the cross section. Table 7.6 shows the effect of these and other corrections for different transverse momentum values. It is clear that the momentum calibration has the largest impact at all transverse momenta.

7.5 Experimental Uncertainties

The experimental uncertainties due to the data selection efficiencies, the luminosity determination and trigger matching, the resolution measurement, the unfolding procedure and the jet energy scale were discussed in previous sections.

Bin Range	Plotted	${\bf Cross~Section~\pm~Statistic}$	Systematic	Num of
(GeV)	$p_T \; ({ m GeV})$	$(\mathrm{nb}/\mathrm{GeV})$	Uncer (%)	Jets
60 - 70	64.6	$8.948E + 00 \pm 5.7E - 02$	-13.5, +14.1	29204
70 - 80	74.6	$3.781E + 00 \pm 3.7E - 02$	-13.6, +14.0	12215
80 - 90	84.7	$1.776E + 00 \pm 2.5E - 02$	-13.8, +14.0	5695
90 - 100	94.7	$8.860E - 01 \pm 1.8E - 02$	-13.9, +14.0	2826
100 - 110	104.7	$4.681E - 01 \pm 3.6E - 03$	-14.1, +14.0	19176
110 - 120	114.7	$2.689E - 01 \pm 2.7E - 03$	-14.3, +14.0	10983
120 - 130	124.8	$1.537E - 01 \pm 2.0E - 03$	-14.5, +14.1	6261
130 - 140	134.8	$9.194E - 02 \pm 1.6E - 03$	-14.7, +14.2	3739
140 - 150	144.8	$5.772E - 02 \pm 1.2E - 03$	-14.9, +14.3	2344
150 - 160	154.8	$3.577E - 02 \pm 2.9E - 04$	-15.1, +14.4	17236
160 - 170	164.8	$2.391E - 02 \pm 2.3E - 04$	-15.3, +14.5	11510
170 - 180	174.8	$1.568E - 02 \pm 1.9E - 04$	-15.5, +14.6	7546
180 - 190	184.8	$1.057E - 02 \pm 1.6E - 04$	-15.8, +14.8	5085
190 - 200	194.8	$7.142E - 03 \pm 1.3E - 04$	-16.0, +15.0	3434
200 - 210	204.8	$4.993E - 03 \pm 8.2E - 05$	-16.2, +15.2	4050
210 - 220	214.8	$3.459E - 03 \pm 6.8E - 05$	-16.5, +15.4	2806
220 - 230	224.8	$2.434E - 03 \pm 5.7E - 05$	-16.7, +15.7	1975
230 - 250	239.4	$1.502E - 03 \pm 3.2E - 05$	-17.1, +16.0	2438
250 - 270	259.4	$7.521E - 04 \pm 2.3E - 05$	-17.6, +16.6	1222
270 - 290	279.5	$4.075E - 04 \pm 1.7E - 05$	-18.1, +17.3	663
290 - 320	303.8	$1.913E - 04 \pm 9.3E - 06$	-18.8, +18.3	468
320 - 350	333.9	$7.616E - 05 \pm 5.9E - 06$	-19.6, +19.7	187
350 - 410	375.8	$2.366E - 05 \pm 2.3E - 06$	-20.9, +21.9	117
410 - 560	461.8	$1.189E - 06 \pm 3.3E - 07$	-23.8, +27.9	15

Table 7.5: Inclusive cross section with jets reconstructed using the k_{\perp} algorithm in the central pseudo-rapidity region.

Correction	60 GeV	100 GeV	$400~{ m GeV}$
Calorimeter Cell Restoration	2%	3.5%	3%
H_T	3%	3.5%	5%
EMF, CHF, $\not\!\!E_T$ Cut Efficiencies	0.2%	0.3%	1%
Vertex Cut Efficiency	10%	10%	10%
Unsmearing	8%	5.5%	7%
Momentum Calibration	50%	40%	45%

Table 7.6: Approximate size of the different corrections to the inclusive jet cross section for three transverse momentum values.

Figure 7.8 presents the fractional experimental errors in the cross section as a function of jet transverse momentum. Also shown is the total uncertainty calculated as the quadrature sum of the different sources. The momentum scale contribution dominates at medium and high momentum (the error on the transverse momentum is of the order of 1.5-5%, which corresponds to 8-25% on the cross section). At low momentum the luminosity uncertainty is of the same order than the momentum scale error.

The error sources relevant to this analysis, with their degree of correlation, are listed in Table 7.7. The momentum scale response correction, the largest source of error at high momentum, is obtained from a fit to data as a function of jet momentum. The error to the jet response function was derived in [41]. The correlation matrix has been obtained for the same 24 bins of partially corrected momenta that were used to determine the cross section. For a complete discussion of the uncertainty in the cross section due to the momentum scale correction see [42]. The different errors together with their degree of correlation and the statistical uncertainties are combined into the full error matrix.

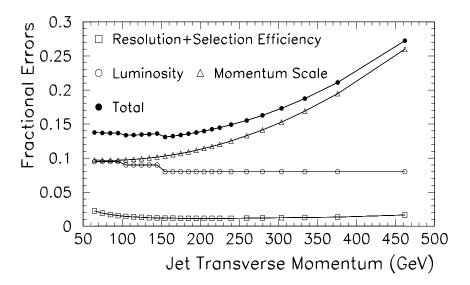


Figure 7.8: Fractional experimental uncertainties on the cross section. The high and low errors are slightly not symmetric, the average is shown in this plot.

Error Source	Correlation	Order of
	$(\mathbf{in}\ p_T\)$	Magnitude
Statistical	${\bf uncorrelated}$	0.5 - 25%
Luminosity	$\operatorname{correlated}$	8%
Luminosity Matching		
Jet_30	Stat, Correlated	1.8%
Jet_50	between triggers	1.3%
Resolution + Unfold	$\operatorname{correlated}$	$\geq 4\%$
Select Efficiencies	$\operatorname{correlated}$	$\geq 2\%$
Mom Scale Response Fit	partially corr	1.5 - 20%
Mom Scale Offset Errors	$\operatorname{correlated}$	7 - 15%

Table 7.7: Sources of errors of the cross section and their degree of correlation. See [41] for a detailed explanation of the momentum scale errors.

Chapter 8

Comparison with Theory and Analysis of the Results

This chapter presents the comparison of the inclusive k_{\perp} jet cross section to NLO QCD predictions with different parton distribution functions. The differences between the data and the theory are discussed qualitatively and a full χ^2 analysis is presented. This is followed by a comparison of the k_{\perp} and cone jet cross sections, which introduces studies of k_{\perp} and cone jets, both in data and Monte Carlo samples, aimed at understanding the differences between the two cross sections.

8.1 Data and Theory Comparison

This section presents the comparison of the k_{\perp} jet inclusive cross section to NLO QCD predictions. Figure 8.1 presents the difference between the data (D) and JETRAD theoretical predictions (T) normalized to the prediction (ie, (D-T)/T). Also shown are the statistical error bars and systematic uncertainty band. Theoretical predictions were generated using the parton distribution functions (PDF's) MRST(98), MRSTg \uparrow (98), MRSTg \downarrow (98), CTEQ3M, CTEQ4M and CTEQ4HJ. In all cases the renormalization and factorization scales were set to $p_T^{max}/2$.

Visually, form Figure 8.1, the theoretical predictions exhibit a normalization difference from data of about 20%, and a bigger discrepancy at low momenta. A more quantitative measure of the agreement or disagreement between data and theory is given by the χ^2 test:

$$\chi^2 = \sum_{ij} (D_i - T_i) C_{ij}^{-1} (D_j - T_j)$$
(8.1)

where $(D_i - T_i)$ is the difference between the measured cross section (D_i) and the theoretical prediction (T_i) in the i-th bin, and C_{ij} is the error matrix of the measurement. The error matrix is obtained from the absolute errors of the measurement and the fractional, systematic, errors (see section 7.5).

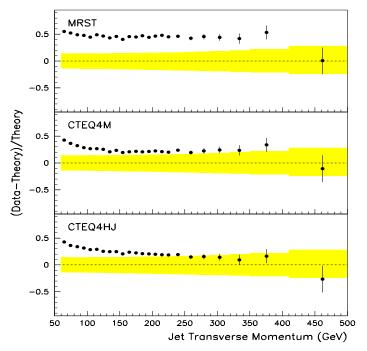


Figure 8.1: Comparison of the central inclusive jet cross section and NLO JETRAD predictions ($\mu = 0.5 \times p_T^{max}$).

The "standard" χ^2 definition (std), used in DØ's cone cross section first published results [60, 61], in which the systematic uncertainties are calculated using

the observed cross section per bin:

$$C_{ij} = C_{ij}^A + C_{ij}^F D_i D_j (8.2)$$

where C^A corresponds to the absolute errors and C^F to the fractional ones, introduces a statistical component to the systematic uncertainty [15]. When the measured cross section fluctuates high, the systematic uncertainties also fluctuate to larger values. Therefore a factor that favors larger measurements is introduced into the χ^2 calculation. To remove this bias a modified definition of the χ^2 was considered [15]:

$$C_{ij} = C_{ij}^A + C_{ij}^F T_i T_j (8.3)$$

The systematic uncertainty is given by the fractional errors multiplied by the theoretical predictions. Table 8.1 shows the χ^2 values for the comparison between data and different theories. All fits have 24 degrees of freedom. The NLO theories differ only by the choice of the parton distribution function. The χ^2 results for both definitions, equations 8.2 and 8.3, are listed for comparison, but hereafter the latter definition is adopted.

PDF	χ^2	Prob (%)	$\chi^2 \; ({ m std})$	Prob (%)
	(ndof=24)		(ndof=24)	
MRST	26.8	31.0	21.7	59.8
MRSTg↑	33.1	10.3	26.5	33.0
MRSTg↓	28.2	25.1	20.2	68.4
CTEQ3M	37.5	4	33.0	10.3
CTEQ4M	31.2	15	26.4	33.2
CTEQ4HJ	27.2	29	24.3	44.1

Table 8.1: Results of the χ^2 test using the definitions given by equations 8.3 and 8.2 (std).

In order to determine the significance of the difference between data and theory at low transverse momentum, Table 8.2 lists the χ^2 results for the last 20 bins, while Table 8.3 includes only the first four points. The last 20 bins show total consistency between the data and the theory (the probabilities are, as expected, around 50%). It is clear that the deviations at low p_T are important, with negligible probabilities that the degree of discrepancy observed is due to a statistical fluctuation. This merits further studies that will be carried along two lines: (a) comparison to previous cone cross section results, where this deviation at low p_T does not appear and (b) critical revision of detector effects and assumptions in the theoretical prediction.

PDF	χ^2	Prob (%)
	(ndof=20)	
MRST	22.9	29.2
MRSTg↑	22.2	32.8
MRSTg↓	25.7	17.4
CTEQ3M	17.4	62.7
CTEQ4M	15.8	72.7
CTEQ4HJ	15.1	77.3

Table 8.2: Results using only the last 20 bins to compute the χ^2 , which corresponds to excluding the JET_30 trigger. The probabilities obtained indicate good agreement between data and theory.

8.2 The Cone Inclusive Jet Cross Section

As it was mentioned before, the previously published $D\emptyset$ cone jet cross section, obtained from essentially the same data sample, does not exhibit a departure between data and theory at low p_T . Before comparing k_{\perp} and cone jets in an attempt to understand this difference, the cone cross section from the $D\emptyset$ fixed data sample (used to determined the k_{\perp} cross section) was reobtained. This data

PDF	χ^2	Prob (%)
	(ndof=4)	
MRST	15.7	0.3
MRSTg↑	22.2	0.02
MRSTg↓	16.4	0.2
CTEQ3M	21.7	0.02
CTEQ4M	20.5	0.04
CTEQ4HJ	18.2	0.1

Table 8.3: Results using only the first 4 bins (which correspond to the JET_30 trigger) to compute the χ^2 . Only for some PDF's a marginal agreement is attained.

sample, although similar to the one previously used, exhibits some differences in the way it was reconstructed and selected (see section 3.2.3).

In order to obtain the DØfixed cone cross section, the corrections for the AIDA suppressed cells and the misidentified primary vertices were applied (see sections 3.2.4 and 3.2.5), then the energy of the cone jets was corrected to particle level using the program CAFIX 5.1 [48]. The missing E_T cut applied was $R_{MTE} < 0.7$ with an efficiency of 99.8% and the same vertex cut efficiency and quality cuts as for the k_{\perp} cross section were applied. The efficiencies were extracted from the previous non DØfixed result [45]. The cone jet energy resolution determination is described in section 6.3.1. The luminosities as described in section 7.1 were used.

Table 8.4 lists the DØfixed reobtained cone cross section, and the number of jets per bin. For comparison, also tabulated are the number of jets from the non DØfixed published paper [15]. Note that it has not been our intention here to exactly reproduce the previous cone result. Not only there are differences in the actual number of events and reconstruction procedures for the DØfixed and non DØfixed samples, but also a separate energy calibration (CAFIX version 5.2^1) and a missing E_T cut ($E_T < max(30 \, GeV, 0.3 \, E_T^{lj})$) was used for the non DØfixed

¹CAFIX versions 5.1 and 5.2 differ in the showering corrections [62].

Bin Range	Plotted p_T	Cross Section	Num of	Num of Jets	This result
(GeV)	(GeV)	$(\mathrm{nb}/\mathrm{GeV})$	Jets	not DØ	/Previous
				Fixed [45]	(Num of Jets)
60 - 70	64.6	6.914E + 00	22956	22627	1.01
70 - 80	74.6	3.005E + 00	9847	9642	1.02
80 - 90	84.7	1.464E + 00	4750	4594	1.03
90 - 100	94.7	7.141E - 01	29655	30208	0.98
100 - 110	104.7	3.971E - 01	16398	16311	1.01
110 - 120	114.7	2.277E - 01	9360	9288	1.01
120 - 130	124.8	1.295E - 01	5304	5316	1.00
130 - 140	134.8	7.717E - 02	37582	38318	0.98
140 - 150	144.8	4.954E - 02	24073	24161	1.00
150 - 160	154.8	3.148E - 02	15268	15206	1.00
160 - 170	164.8	2.032E - 02	9843	9951	0.99
170 – 180	174.8	1.365E - 02	11195	11416	0.98
180 - 190	184.8	9.119E - 03	7474	7819	0.96
190 - 200	194.8	6.136E - 03	5026	5282	0.95
200 - 210	204.8	4.328E - 03	3544	3595	0.99
210 - 220	214.8	2.933E - 03	2401	2574	0.93
220 - 230	224.8	2.118E - 03	1734	1869	0.93
230 - 250	239.4	1.243E - 03	2036	2265	0.90
250 - 270	259.4	6.592E - 04	1081	1148	0.94
270 - 290	279.5	3.641E - 04	598	659	0.91
290 - 320	303.8	1.716E - 04	424	478	0.89
320 - 350	333.9	6.523E - 05	162	187	0.87
350 - 410	375.7	1.775E - 05	89	103	0.86
410 - 560	461.2	1.241E - 06	16	20	0.80

Table 8.4: Inclusive cone jet cross section from $D\emptyset$ fixed data. The last column shows the comparison between the cone $D\emptyset$ fixed result, and the previous, non $D\emptyset$ fixed result from [15]. There is excellent agreement between the two.

data. However it is important that, except for minor variations, the global features of the published cone result have been reproduced here with a differently processed data sample and analysis procedure. This is both an important cross-check of our method, and it indicates that the distinct behavior of the cone and k_{\perp} cross section at low p_T is not due to the different analysis path followed.

8.3 k_{\perp} and Cone Jets at High p_T

In general, the k_{\perp} and cone cross sections can only be compared on a bin by bin basis, and not event by event, due to the high statistics involved in this experiment. The highest p_T bin is however an exception, for it contains 20 entries in the published cone result [45] while only 15 k_{\perp} jets in the analysis here presented (both use the same p_T binning). These are small numbers, which permit to separately track the fate of each jet in an attempt to understand the origin of the difference.

We find that all 15 jets of the last bin in the k_{\perp} cross section are present in the last bin for the cone case. Of the 5 missing jets, three turn out to have lower energy and are found in the previous bin, one falls out of the pseudo-rapidity acceptance ($\eta = 0.51$ in the k_{\perp} case, $\eta = 4.7$ for cone) and one has a different vertex Z position, which in the case of the k_{\perp} case is selected because it minimizes H_T , but gets discarded because it falls out of the Z acceptance region. Table 8.5 summarizes this information. It is interesting to remark that the same 20 high p_T objects have been independently found by both algorithms out of the millions of events taken during the run. The realization that they have somewhat different kinematics points to the inherent difference between the k_{\perp} and cone algorithms and the fact that jets are not primary physics objects but algorithm dependent.

Run	Event	Cone E_T	$k_{\perp} p_T$	
number	Number	(not DØfixed)	(DØfixed)	
72738	10623	453.35	447.16	
78535	5137	415.69	417.36	
78535	5137	465.98	469.25	
82238	9375	421.35	421.09	
83027	20229	429.57	423.81	
86256	4229	444.57	438.75	
86722	22136	416.22	414.04	
87225	3342	488.75	481.85	
87428	16996	420.62	419.44	
87428	16996	437.39	_	$\eta = 0.51$
87481	23178	411.80	402.89	to lower bin
87481	23178	450.22	429.41	
90349	37817	420.11	_	≠ vtx_z2
90808	29489	421.38	420.62	
90915	23531	417.89	440.21	
91208	184	413.92	369.58	to lower bin
91876	30511	419.16	422.34	
91923	6616	411.10	438.78	
91923	6616	444.51	443.76	
92703	35465	411.84	408.39	to lower bin

Table 8.5: Highest p_T jets for k_{\perp} and cone (not DØfixed). The energies are corrected using CAFIX 5.2 for cone and KTFIX 1.0 for k_{\perp} jets [41].

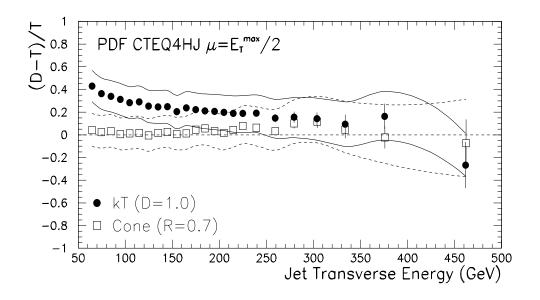
8.4 k_{\perp} and Cone Jet Cross Sections

Having gained confidence that the unsimilar behavior between k_{\perp} and cone is not an analysis artifact, we proceed to study the comparisons of the k_{\perp} and cone cross sections to their respective theoretical predictions. Figure 8.2 shows the comparisons between NLO QCD predictions, with the CTEQ4HJ PDF and $\mu = E_T^{max}/2$, and the k_{\perp} (D=1.0) and cone (R=0.7) [61] results in the central rapidity region ($|\eta| < 0.5$). Both cross sections were calculated using the same bins in transverse energy. Note that there is only one source of systematic error that is common to both samples, the luminosity. For showering and misclustering corrections there is no correlation, while for other sources (e.g., response and offset) the degree of correlation has not been studied in depth but is expected to be marginal.

As it has already been discussed in chapter 1, the NLO predictions for the inclusive cross section for k_{\perp} jets with D=1 and cone jets with R=0.7 agree within a few percent. Nonetheless, Figure 8.2 indicates that while there is reasonable agreement at high p_T between the cone and k_{\perp} cross sections, there is a clear difference at low transverse momentum. Since the events are basically the same, this difference originates because either there are more k_{\perp} than cone jets per event or because k_{\perp} jets are more energetic. A natural way to study this is to compare the energy of single k_{\perp} and cone jets. This can be done by matching in $\eta - \phi$ space k_{\perp} and cone jets in the same event. This issue is discussed in the following sections.

8.4.1 Comparing individual k_{\perp} and Cone Jets in the Data

In an effort to understand the differences between the cone and k_{\perp} cross sections, jets reconstructed with the different algorithms (using the k_{\perp} DØfixed data sample) were matched in $\eta - \phi$ space and their difference in transverse energy plotted as



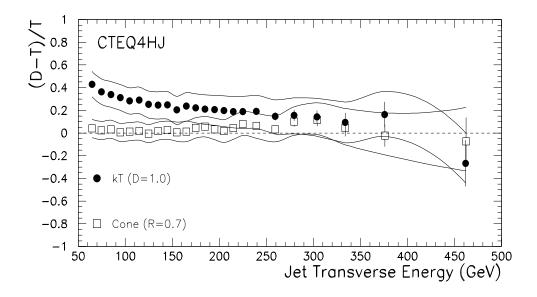


Figure 8.2: Comparisons of the k_{\perp} and cone [61] cross sections with theory (obtained using the JETRAD program with the CTEQ4HJ PDF and $\mu = E_T^{max}/2$). The plot below does not include the luminosities uncertainties, as they are fully correlated between cone and k_{\perp} .

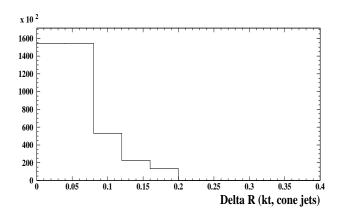


Figure 8.3: Distance in $\eta - \phi$ space between two leading k_{\perp} and cone jets.

a function of k_{\perp} jet p_T . The AIDA cell restoration algorithm was applied and the vertex which minimized the missing H_T was selected. All jets had to satisfy the quality cuts and their pseudo-rapidity fall in the central region of the detector ($|\eta| < 0.5$). Cone jet energies were corrected using CAFIX 5.1 while KTFIX was used to correct the momentum of the k_{\perp} jets [41]. The two leading cone jets were matched to the two leading k_{\perp} jets in $\eta - \phi$ with $\Delta R = \sqrt{\delta \phi^2 + \delta \eta^2} < 0.2^2$. Figure 8.3 shows the spatial separation between the leading k_{\perp} and cone jets and Figure 8.4 the average E_T difference, $\Delta E_T^{avg} = \langle p_T^{kT} - E_T^{cone} \rangle$, as a function of jet momentum for the four triggers used in this analysis. There is a systematic upward energy shift of k_{\perp} jets over cone jets, which decreases with energy ($\sim 6.5\%$ at 65 GeV and $\sim 3\%$ at 205 GeV).

The k_{\perp} (cone) momentum (energy) scale uncertainty in the central region is of the order of 1.5% (1.5%) for jet $p_T > 60$ GeV. Since the biggest source of uncertainty in the cone jet energy comes from the out of cone showering correction, which is absent in k_{\perp} jets, while the k_{\perp} momentum correction has a misclustering uncertainty which is not present in the cone correction, it will be assumed that

²The value of this cut was varied between 0.05 and 0.3 with no significant difference in the results.

the k_{\perp} and cone energy scale uncertainties are uncorrelated. Thus, the observed difference between matched k_{\perp} and cone jet p_T 's has an uncertainty of the order of 2% above 60 GeV, as shown in Figure 8.4.

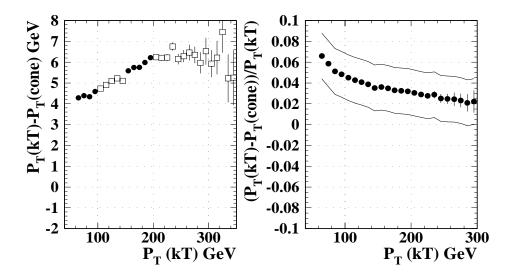


Figure 8.4: The plot on the right shows the average E_T difference for matched k_{\perp} and cone jets, on the left the difference is normalized by the k_{\perp} jet's transverse momentum. Each trigger, indicated by the different symbols on the plot on the left, is plotted in the same p_T range in which it was used in the cross section. The systematic error band, shown in the plot on the right, originates from the k_{\perp} and cone energy scales uncertainties (see text).

It can be shown that the higher energy of the k_{\perp} jets can quantitatively account for the difference between the k_{\perp} and cone cross sections. Propagating the energy shift between k_{\perp} and cone jets into the cross section, which roughly depends on p_T like p_T^{-5} , we predict that, at 65 (205) GeV, the k_{\perp} cross section will be 33% (15%) higher than the cone one. Figure 8.5 compares the (D-T)/T plot for k_{\perp} with the result of shifting the experimental cone cross section (from [61]) by $\Delta E_T = \Delta E_T^{avg}$, as a function of E_T cone, for each E_T region where the trigger is fully efficient. Figure 8.5 indicates that the energy difference between matched k_{\perp} and cone jets alone (and not, for example, the number of jets per bin) explains the different measured cross sections for the $k_{\perp}(D=1)$ and cone (R=0.7) algorithms. However, this explanation should be taken with care as only 66% of the jets contributing to the cross section are matched, and the matching requirement could introduce biases (narrower jets are matched more often, they have a better response and thus the energy correction would be overestimated).

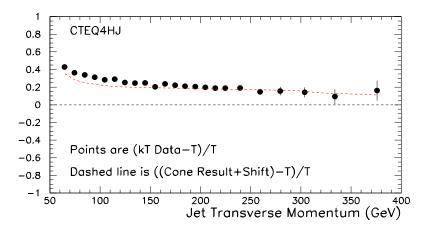


Figure 8.5: k_{\perp} "predicted" and data cross sections compared with theory. The k_{\perp} prediction is obtained by shifting the cone fit to the data (from [61]) by the average difference in E_T between matched k_{\perp} and cone jets.

k_{\perp} and Cone Offset Corrections

At this point a natural question that arises is whether k_{\perp} jets are genuinely more energetic than cone ones, or if this difference is due to an experimental artifact, like an underestimation of the offset correction to k_{\perp} jets.

Figure 8.6 shows that k_{\perp} jets have a larger contribution from the detector environment (zero bias offset). At central pseudo-rapidities, the O_{zb} for k_{\perp} jets is about 60% larger than for cone jets. The underlying event offset is also larger for k_{\perp} jets, about 35% (with little dependence on transverse energy), as shown

in Figure 8.7. This last result has been verified using HERWIG Monte Carlo simulations, see appendix B. So k_{\perp} jets have a larger contribution from both the detector environment and the underlying event, while the uncertainty is basically the same [41]. This is an indication that k_{\perp} jets with D=1 encompass more energy than cone jets with R=0.7, as has already been determined by matching k_{\perp} and cone jets in the data.

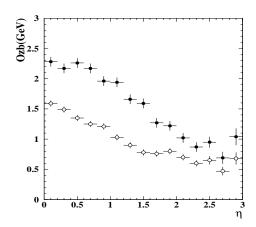


Figure 8.6: O_{zb} contribution to the offset for k_{\perp} , D=1, (full circles) and cone, R=0.7, jets.

It is interesting to note that the energy shift between k_{\perp} and cone jets does not depend on on the instantaneous luminosity, as it is shown in Figure 8.8. This

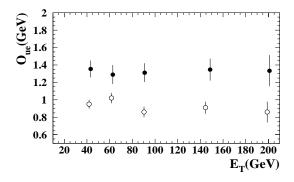


Figure 8.7: O_{ue} contribution to the offset for k_{\perp} , D=1, (full circles) and cone, R=0.7, jets.

is an important check of the offset correction, since the contribution to the offset from the overall detector environment is luminosity dependent. If the offset due to the overall detector environment (O_{zb}) were wrong for k_{\perp} and right for cone, then it would have shown as a luminosity dependence in Figure 8.8.

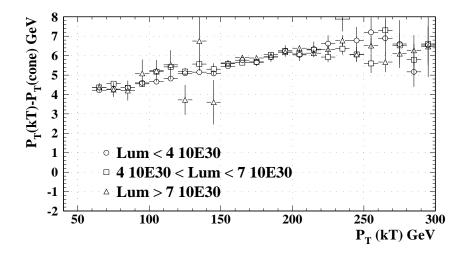


Figure 8.8: Average E_T difference for matched k_{\perp} and cone jets, for different luminosities (in units of cm⁻²sec⁻¹). Only statistical errors are included.

8.4.2 Comparing individual k_{\perp} and Cone Jets in Monte Carlo

In order to investigate further the energy difference between k_{\perp} and cone jets in the data, a similar study was carried out using a particle level Monte Carlo HERWIG [29] sample. Since the reconstructed jet energy (momentum) is corrected back to particle level, the particle level Monte Carlo jet sample should also indicate that cone (R=0.7) jets are less energetic than k_{\perp} jets (D=1.).

A HERWIG Monte Carlo sample, with no underlying event³, was used to study the energy difference between k_{\perp} and cone jets at particle and parton levels. Fi-

³See appendix B for a discussion about the underlying event.

gure 8.9 shows the E_T ratio of the matched jets. At particle level there is an upward energy shift of k_{\perp} jets with respect to cone ones, about $\sim 2\%$ at 65 GeV and $\sim 1\%$ at 205 GeV, which propagated into the cross section would account for a 10% (5%) difference at 65 (205) GeV. Note that this shift agrees, within energy scale errors, with the one obtained from data for jet $p_T > 120$ GeV. The absence of a shift at parton level is in agreement with the fact that NLO QCD predicts the same cross section for k_{\perp} and cone jets. It also hints that the difference in energy at particle level is due to the process between partons and particles, that is, the hadronization step, a contribution that was usually regarded as non-important.

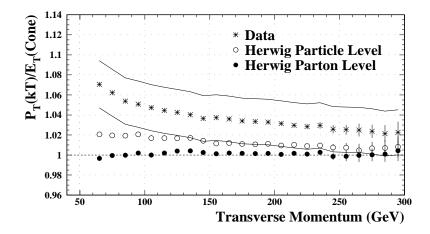


Figure 8.9: Ratios of the transverse momentum of matched k_{\perp} and cone jets from a particle level (open circles) and parton level (full circles) HERWIG sample. Also shown is the result from data (asterisks).

8.4.3 Comparing global production of k_{\perp} and Cone Jets in Monte Carlo

As mentioned before, conclusions drawn from the energy difference of matched jets should be taken with care, as the matching process could selectively choose jets with peculiar properties. In order to test the argument presented in the previous section we look here at the ratio of the p_T spectra of all the leading jets, k_{\perp} over cone, with no matching requirement, from a HERWIG Monte Carlo sample The result is shown in Figure 8.10. Again, there is an energy shift for particle jets but not for parton jets, in reasonable agreement with Figure 8.9 which required jets to be matched: at 65 GeV (200 GeV), Figure 8.9 predicts a $\sim 10\%$ ($\sim 5\%$) ⁴ difference between the k_{\perp} and cone cross sections, which is consistent with the result of 9% (3.5%) obtained without a matching requirement in Figure 8.10.

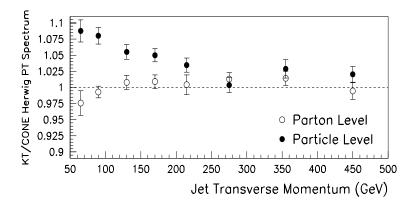


Figure 8.10: Ratios of k_{\perp} over cone jet p_T spectra for particle (full circles) and parton (open circles) level HERWIG Monte Carlo as a function of $k_{\perp} p_T$ (no underlying event overlayed).

8.5 Hadronization Effects

Theoretical calculations at NLO predict a similar cross section for k_{\perp} (D=1) and cone ($R=0.7, R_{sep}=1.3$) jets (section 1.5.1). However, we have shown (section 8.4.2) that while Monte Carlo simulations indicate that k_{\perp} parton and cone jets have similar energy, k_{\perp} particle jets encompass more energy than cone

⁴Figure 8.9 indicates that at 65 GeV k_{\perp} jets are a 2% more energetic than cone jets, this 2% propagated to the cross section ($\sigma \sim p_T^{-5}$) predicts a 10% difference.

jets, a fact also supported by the data (section 8.4.1). This motivates the study of how hadronization, the process mediating the step between partons and particles, affects the different kind of jets and their respective cross section theoretical predictions.

Monte Carlo Evidence

In Monte Carlo samples, instead of matching cone and k_{\perp} jets, parton and particle jets can be compared within each algorithm. Figure 8.11 shows, for both algorithms, the transverse momentum ratios of the matched particle to parton jets as a function of the p_T of the parton jet. It is interesting to note that HERWIG, which at parton level corresponds to LO predictions plus parton showering, while at particle level it incorporates hadronization, predicts that cone particle jets loose energy, in agreement with [63], while k_{\perp} jets gain energy. At 65 (200) GeV Figure 8.11 indicates that k_{\perp} particle jets are $\sim 2\%$ ($\sim 1\%$) more energetic than cone jets, in agreement with Figure 8.9.

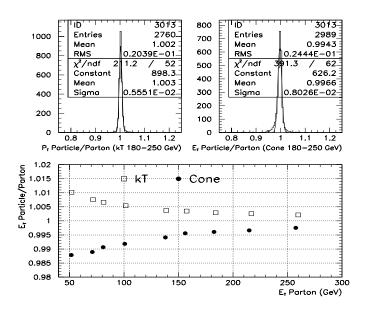


Figure 8.11: Ratios of matched particle to parton E_T as a function of parton E_T for cone and k_{\perp} jets ($|\eta| < 0.5$) from HERWIG.

As mentioned above, section 8.4.1, the matching process could introduce biases in the comparisons between different types of jets. To avoid this requirement the ratio of p_T spectra of the two leading particle to parton level jets, for both the k_{\perp} (D=1.0) and cone (R=0.7) algorithms, is studied, see Figure 8.12. As in Figure 8.11, particle cone jets reconstructed from final state particles (after hadronization), have less p_T than the parton jets (before hadronization), while k_{\perp} particle jets are more energetic than their progenitors at parton level⁵ (as the two leading jets are used in each case, the number of jets is the same).

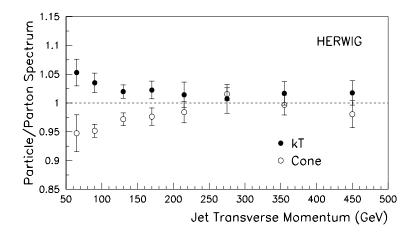


Figure 8.12: Ratios of HERWIG particle over parton level spectra for k_{\perp} (full circles) and cone (open circles) jets as a function of parton E_T (no underlying events overlayed).

Origin of the Hadronization Effect

The previous section shows that the hadronization step affects in a different way k_{\perp} and cone jets. In this section we try to understand the origin of this effect using a Monte Carlo sample.

⁵Note that Figure 8.11 indicates that k_{\perp} particle jets are 1% more energetic than parton jets at 60 GeV, this, propagated into the cross section, implies a $\sim 5\%$ effect as shown in Figure 8.12.

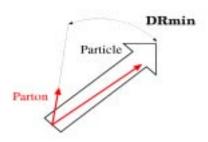


Figure 8.13: DRmin is the distance between the leading parton jet to the closest parton jet with $p_T > 8$ GeV. The ratio between the leading particle (open arrow) to the corresponding parton jet is plotted against DRmin in Figure 8.14.

To understand the effect of hadronization on k_{\perp} and cone jets, the transverse momentum of the leading particle jet was divided by the p_T of the corresponding (matched) parton jet. This ratio was plotted against DRmin, which is the $\eta - \phi$ distance to the closest parton jet, with $p_T > 8 \text{ GeV}^6$ (see Figure 8.13). The result, for both k_{\perp} and cone jets, for the HERWIG sample with generation thresholds of 50 and 75 GeV is plotted in Figure 8.14. The p_T cut of 8 GeV was imposed to both k_{\perp} and cone jets.

The cone result on Figure 8.14, which indicates that particle cone jets are less energetic than parton jets, can be explained as "physics" out of cone showering, ie, particle jets do not contain the full result of the showering and hadronization process. The result at low distances (DRmin ~ 0.7) has to be taken with care as splitted and merged jets are involved. The second plot of Figure 8.14 explains why k_{\perp} particle jets are more energetic than their corresponding parton jet. When the closest parton jet is further than DRmin ~ 1.5 in $\eta - \phi$ space the ratio of particle over parton jets is below but almost one. But when the closest parton jet is close to the leading parton jet (DRmin < 1.5) these are merged into a single particle jet and thus the ratio particle over parton p_T increases above one. This same argument – the merging of nearby parton jets into one particle jet – is valid for

 $^{^6\}mathrm{A}$ cut of 5 GeV was also studied (for k_\perp) with no significant difference in the results.

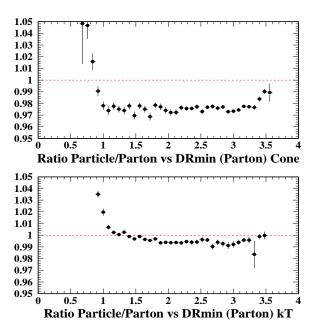


Figure 8.14: Ratio of HERWIG leading particle over parton jet p_T as a function of the distance of the closest parton jet to the parton one used for the ratio (DRmin), for cone jets (above) and k_{\perp} jets (below). The generation thresholds of the samples used to produce these plots were 50 and 75 GeV.

cone jets as well, but from the top plot of Figure 8.14 one concludes that the "out of cone showering" effect dominates.

If this interpretation of the k_{\perp} results is correct then one would expect that the ratio of the leading particle jet p_T over the sum of the transverse momenta of the leading and the closest to the leading parton jets, would flatten to one at low DRmin values. This is exactly what it is observed, see Figure 8.15.

Finally, one must note that the actual effect of hadronization in the p_T difference between particle and parton level jets depends, not only on the algorithm's parameters, but also on the details of the algorithms $per\ se$; cone algorithms suffer from out of cone showering effects, which are absent in the k_{\perp} algorithm.

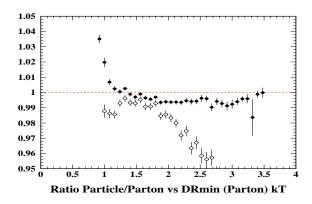


Figure 8.15: Ratio of HERWIG leading particle over parton k_{\perp} jet p_T as a function of DRmin (full circles). The open circles correspond to the ratio of leading particle jet p_T over the p_T sum of the leading parton and the closest parton to the leading one as a function of DRmin. The generation thresholds of the samples used to produce this plot were 50 and 75 GeV.

8.5.1 Including Hadronization in the NLO QCD Theoretical Predictions

Having shown that the k_{\perp} and cone algorithms show different sensitivity to the hadronization process, it is interesting to study how the theoretical NLO perturbative QCD prediction gets modified by hadronization and to what extent this affects the partial disagreement observed at low p_T . To this end, the NLO prediction of the k_{\perp} jet cross section is corrected using the difference between parton and particle jets as determined from the HERWIG simulation. We observe that, for the MRST (CTEQ4HJ) PDF, the agreement between the measurement and prediction improves to 46% (44%) probability. This is summarized in Table 8.6, which lists the χ^2 results with and without including the hadronization from HERWIG in the prediction, and in Figure 8.16, which shows the corresponding ratios of (D-T)/T. We thus conclude that hadronization can explain some of the difference between the data and the NLO QCD predictions, and the it affects basically the low p_T region.

PDF	χ^2	Prob (%)
	(ndof=24)	
MRST+hadroniz.	24.0	46
CTEQ4HJ+hadroniz.	24.3	44
MRST	26.8	31
CTEQ4HJ	27.2	29

Table 8.6: χ^2 comparisons (24 degrees of freedom) between JETRAD, including a hadronization correction obtained from HERWIG, and data (with renormalization and factorization scales set to $p_T^{max}/2$). Also shown are the results without the hadronization correction.

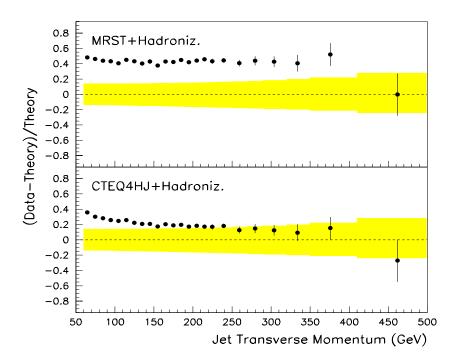


Figure 8.16: Comparison of the central inclusive jet cross section and NLO jetrad predictions modified to include the difference between particle and parton jets from Herwig ($\mu = 0.5 \times p_T^{max}$).

8.6 Conclusions

The first measurement of the inclusive jet cross section using the k_{\perp} algorithm in proton-antiproton collisions at $\sqrt{s} = 1.8$ TeV was presented. Quantitative tests show reasonable agreement between data and NLO QCD predictions, except at low p_T where the agreement is marginal.

In order to study the difference between the measured cross section and the NLO predictions at low p_T , comparisons between the k_{\perp} and the cone results, which do not present this deviation, were pursued. A difference as high as 37% at low transverse momenta (decreasing with p_T) between the cone and k_{\perp} cross sections was found. By comparing individual k_{\perp} and cone jets, it was determined that the difference between the k_{\perp} and cone cross section measurements is explained by the energy difference between matched k_{\perp} and cone jets. Several studies were performed in order to determine that this energy difference was not caused by an experimental artifact.

Monte Carlo simulations using the HERWIG program, which at particle level includes a LO prediction with parton shower and hadronization, also show higher particle jet energies for k_{\perp} than cone jets, consistently with data. We show that this is reasonably explained by how the two algorithms are sensitive to the shower spreading that takes place during hadronization. Theoretical predictions at NLO of the inclusive jet cross section using the cone algorithm to reconstruct jets, with R=0.7 and $R_{sep}=1.3$, agree, within a few percent, with the predictions using the k_{\perp} algorithm with D=1.0. But this does not mean that at all orders the k_{\perp} and cone cross sections should give the same result. It was determined that the difference between k_{\perp} particle-level and parton-level p_T spectra predicted by HERWIG, which takes account of hadronization, can explain some of the difference between the k_{\perp} data and NLO predictions at low p_T .

Appendix A

Preclustering Studies

As described in section 1.3.3, as a consequence of limited computer power, the input to the k_{\perp} algorithm is a list of preclusters and not the total number of towers of the calorimeters. In this section, using Monte Carlo samples, the effect of preclustering on the jet momentum spectrum is studied. Ideally, these studies would be based on a calorimeter simulation of the detector, however, computer power constraints make this option not available. Therefore, particle level simulation is used instead.

Two HERWIG Monte Carlo samples, of 5000 events each, with different preclustering parameters were produced. The events were generated with minimum leading parton $p_T > 50$ GeV and the jets were reconstructed using the k_{\perp} algorithm with D=1. Zero bias events with a luminosity of $L=3\times 10^{30}$ cm⁻² s⁻¹ were overlaid. The preclustering parameters of each sample were $\Delta R=0.1$ and $p_T^{min}=120$ MeV (sample A), and $\Delta R=0.3$ and $p_T^{min}=300$ MeV (sample B). Recall that the data was preclustered with $\Delta R=0.2$ and $p_T^{min}=200$ MeV (see section 3.2.3). Figure A.1 shows the p_T spectra of the two leading jets, for parton and particle level, using the different preclustering parameters. The effect on the mean of the distributions is very small. A better comparison is obtained by matching, in $\eta - \phi$ space, the two leading parton jets to the closest particle jet and calculating the

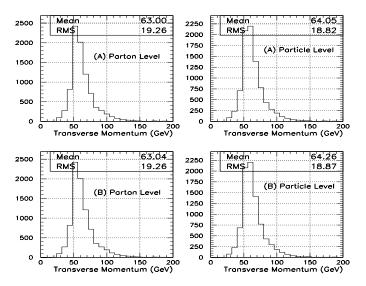


Figure A.1: Momentum spectra of the two leading parton and particle level jets using different preclustering parameters (see text).

difference in p_T and a function of the particle jet momentum for both samples. Figure A.2 shows this plot. Again there is no significant difference between the two preclustering schemes. This result agrees with previous studies [18].

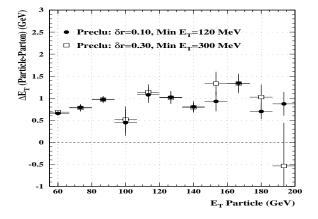


Figure A.2: Energy difference between matched particle and parton level jets for different preclustering parameters.

Appendix B

Underlying Event Correction Studies

This appendix discusses the effect of the background from spectator partons, the underlying event, on the difference in transverse energy between matched particle and parton jets (using HERWIG Monte Carlo simulation) for both, k_{\perp} and cone, algorithms. It also shows that the magnitude of the underlying event correction obtained from minimum bias events (see section 5.1.1) is consistent with HERWIG's predictions.

Because the k_{\perp} and cone energy scale corrections amend for underlying event [41], the results presented in section 8.4.2 were obtained from HERWIG samples with no such background. This also allowed to separate the studies of hadronization and underlying event effects. The consequence of including the underlying event in HERWIG, which affects only the particle level jets, on the energy difference between matched particle and parton jets is shown on Figure B.1 for k_{\perp} and Figure B.2 for cone. These plots indicate that the k_{\perp} algorithm is slightly more sensitive to the effect from the underlying event than the cone algorithm, and in agreement with this result, the underlying event correction (O_{ue}) is larger for k_{\perp} (D = 1.0) than cone (R = 0.7) jets [41].

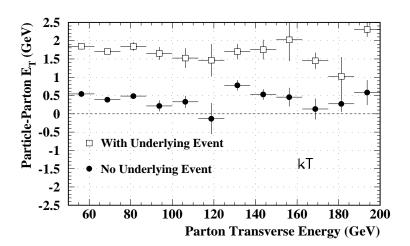


Figure B.1: Effect of the underlying event in the E_T difference between matched parton and particle k_{\perp} jets.

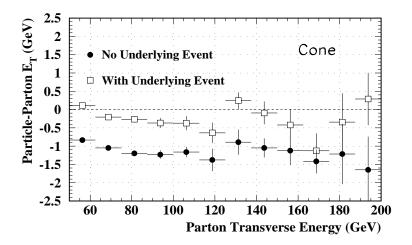


Figure B.2: Effect of the underlying event in the E_T difference between matched parton and particle cone jets.

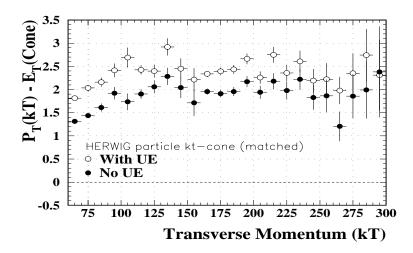


Figure B.3: The average E_T difference for matched k_{\perp} and cone jets at particle level, from a HERWIG Monte Carlo sample with and without underlying event.

The effect of the underlying event on the energy difference between matched cone and k_{\perp} particle jets (HERWIG) is shown in Figure B.3. As expected from Figures B.1 and B.2, the energy difference increases in about ~ 0.5 GeV compared with the same result with no underlying event, also shown in Figure B.3. This figure also indicates that HERWIG predicts, at 60 GeV, an underlying event correction $\sim 35\%$ larger for k_{\perp} jets than cone, in agreement with what was determined from minimum bias events (see section 8.4.1).

Bibliography

- [1] M. Gell-Mann, Phys. Lett. 8, 214 (1964).
- [2] R.E. Taylor, H.W. Kendall and J.J. Friedman, lectures on the occasion of the presentation of the 1990 Nobel Prize in Physics, Rev. Mod. Phys. 63 (1991) 573.
- [3] T. Akesson et al. (AFS Collaboration), Phys. Lett. B 118 (1982) 185.
- [4] S. Catani, Yu.L. Dokshitzer, and B.R. Webber, Phys. Lett. B 285 (1992) 291.
- [5] S. Catani, Yu.L. Dokshitzer, M.H. Seymour, and B.R. Webber, Nucl. Phys. B 406 (1993) 187.
- [6] S. Ellis and D. Soper, Phys. Rev. **D**48 3160 (1993).
- [7] V.M. Abazov *et al.* (DØ Collaboration), Phys. Rev. D 65 (2002) 052008.
- [8] S.L. Glashow, Nucl. Phys. 22, 579 (1961).
 - S. Weinberg, Phys. Rev. Lett. 19, 1264 (1967).
 - A. Salam, in "Elementary Particle Physics", Nobel Symp. No. 8, ed. N. Svartholm, Almqvist and Wilsell, Stockolm (1968).
- [9] K. Hagiwara et al. Phys. Rev. D 66, 010001 (2002).
- [10] V. Barger and R. Phillips, Collider Physics, Frontiers in Physics Lecture Note Series, Addison-Wesley, 1987.

- [11] G.'t Hooft and M. Veltman, Nucl. Phys. B (1972) 189.
- [12] H.L. Lai et al., Phys. Rev. D 55, 1280 (1997).
- [13] T. Affolder et al. (CDF Collaboration), Phys. Rev. D 64, 032001 (2001).
- [14] J. Huth *et al.*, in Proceedings of Research Directions for the Decade, Snowmass, 1990, edited by E.L. Berger (World Scientific, Signapore, 1992).
- [15] B. Abbott et al. (DØ Collaboration), Phys. Rev. D 64, 032003 (2001).
- [16] S.D. Ellis, Talk presented at the XXVIIIth Rencontres de Moriond (1993) hep-ph/9306280.
- [17] M.H. Seymour, presented at the XXXIst Rencontres de Moriond, Moriond, Les Arcs, March 21-28 (1998) hep-ph/9807226.
- [18] G.C. Blazey *et al.*, Proceedings of the Physics at RUN II: QCD and Weak Boson Physics Workshop, Batavia, Illinois, 4-6 Nov (1999) hep-ex/0005012.
- [19] R.M. Snihur, "Subjet Multiplicity of Quark and Gluon Jets Reconstructed with the k_{\perp} Algorithm in $p\overline{p}$ Collisions", Ph.D. Dissertation, Northwestern University, Illinois (2000).
- [20] E. Eichten, K. Lane and M.E. Peskin, Phys. Rev. Lett. 50 (1983) 811.
- [21] S.D. Ellis, Z. Kunszt and D.E. Soper, Phys. Rev. Lett. 64 (1990) 2121.
- [22] W.T. Giele, E.W.N. Glover, and D.A. Kosower, Phys. Rev. Lett. 73, 2019 (1994).
- [23] A. D. Martin *et al.*, Eur. Phys. J. C **4**, 463 (1998).
- [24] N. Glover, "Progress in NNLO calculations for scattering processes", hep-ph/0211412.

- [25] S.D. Ellis, Z. Kunszt and D.E. Soper, Phys. Rev. Lett. 69, 3615 (1992).
- [26] The ZEUS Detector, Status Report (1993), DESY 1993.
 M. Derrick et al. (ZEUS Collaboration), Nucl. Inst. and Methods A 309, 77 (1991).
- [27] M. Klasen and G. Kramer, Phys. Rev. D 56 2702 (1997).
- [28] M.H. Seymour, Nucl. Phys. B 513 (1998) 269.
- [29] HERWIG 5.9, hep-ph/9607393; G. Marchesini (Milano), B.R. Webber (Cambridge), G. Abbiendi (Padova), I.G. Knowles (Glasgow), M.H. Seymour (CERN), L. Stanco (Padova)
- [30] M. H. Seymour, Comput. Phys. Commun. 90 (1995) 95.
- [31] B.R. Webber, Nucl. Phys. B 238 (1984) 492.
- [32] xsection shape of MC....
- [33] J. Thompson, "Introduction to colliding beams at Fermilab", Fermilab Tech. Memo, FERMILAB-TM-1909 (1994).
- [34] S. Abachi et al. (DØ Collaboration), Nucl. Instr. Meth. Phys. in Res. A 338, 185 (1994).
- [35] CERN Courier, Vol. 42, No. 4 (2002).
- [36] R. Brun and F. Carminati, CERN Program Library Long Writeup W5013 (1993).
- [37] W. Dharmaratne, R. Raja and C. Stewart, DØ Internal Note #1730, (1993).
- [38] B. J. May, "Rapidity Gaps between Jets in $p\overline{p}$ Collisions at $\sqrt{s} = 1.8$ TeV", Ph.D. Dissertation (1994).

- [39] B. Abbot, G. Watts, DØ Internal Note \$3006, (1996).
- [40] D. Chakraborty, D0 News # 3750 (1995), http://www-d0.fnal.gov/cgi-bin/d0news?read_GENERAL_3750.
- [41] B. Abbott et. al., DØ Internal Note \$3585, (1999).
- [42] S. Grinstein, D. Elvira and R. Piegaia, DØ Internal Note \$3585, (2001).
- [43] L. Babukhadia et. al., DØ Internal Note \$3408, (1998).
- [44] G. Blazey and R. Hirosky, DØ Internal Note \$3276 (1998).
- [45] L. Babukhadia, "Rapidity Dependence of the Single Inclusive Jet Cross Section in $p\bar{p}$ Collisions at $\sqrt{s} = 1.8$ TeV with the DØ Detector", Ph.D. Dissertation, University of Arizona (1999).
- [46] M. Strang, private communication.
- [47] B. Abbott et. al., Nucl. Instr. and Methods A 424, (1999) 352.
- [48] B. Abbott, et. al., DØ Internal Note \$\pmu 3287, (1997).
- [49] D. Elvira, private communication.
- [50] M. Bhattacharjee, et. al., DØ Internal Note \$2887, (1996).
- [51] I. Bertram, et. al., DØ Internal Note \$3414, (1998).
- [52] D. Elvira, "Measurement of the Inclusive Jet Cross Section at $\sqrt{s} = 1.8 \text{ TeV}$ with the DØ Detector", Ph.D. Dissertation, Universidad de Buenos Aires, (1995).
- [53] S. Grinstein, D. Elvira and R. Piegaia, DØ Internal Note \$3721, (2000).
- [54] L. Babukhadia, private communication.

- [55] J. Bantly, et. al., "D0 luminosity monitor constant for the 1994-1996 tevatron run", Fermilab Tech. Memo, FERMILAB-TM-1995 (1997).
- [56] See http://www-d0.fnal.gov/gris/
- [57] S. Chopra and L. Lueking, private communication.
- [58] G. Lafferty and T. Wyatt, "Where to Stick Your Data Points: The Treatment of Measurements Within Wide Bins", CERN-PPE/94-782, (1994).
- [59] J. Krane, "The Ratio of Inclusive Jet Cross Sections at $\sqrt{s} = 630$ GeV and $\sqrt{s} = 1800$ GeV", Ph.D. Dissertation, University of Nebraska, (1998).
- [60] B. Abbot et. al. (DØ Collaboration), Phys. Rev. Lett. 82 (1999) 2451.
- [61] B. Abbot et. al. (DØ Collaboration), Phys. Rev. Lett. 86 (2001) 1707.
- [62] A. Goussiou, DØ Internal Note \$\\$3606, (1999).
- [63] L. Babukhadia and D. Elvira, DØ Internal Note #3554, (1998).
- [64] K. Frame, "Implementation and Calibration of a k_{\perp} Jet Finding Algorithm For Use in $p\bar{p}$ Collisions at $\sqrt{s} = 1.8$ TeV" Ph.D. Dissertation, Michigan State University, (1999).
- [65] R. Field and D. Stuart, "The Underlying Event in Hard Scattering Processes", contribution to the Run II Workshop on QCD and Weak Boson Physics, Feb 1, 2000.